December 2016

Stationary Nonimaging Concentrators – A Comprehensive Study and Design Improvements

Srikanth Madala
University of Nevada, Las Vegas, srikant.madala@gmail.com

Repository Citation

Madala, Srikanth, "Stationary Nonimaging Concentrators – A Comprehensive Study and Design Improvements" (2016). *UNLV Theses, Dissertations, Professional Papers, and Capstones*. 2877.
https://digitalscholarship.unlv.edu/thesesdissertations/2877

STATIONARY NONIMAGING CONCENTRATORS – A COMPREHENSIVE STUDY AND DESIGN IMPROVEMENTS

By

Srikanth Madala

Bachelor of Technology – Mechanical Engineering
Jawaharlal Nehru Technological University (Hyderabad)
2007

Master of Sciences – Mechanical Engineering
University of Florida
2008

A dissertation submitted in partial fulfillment
of the requirements for the

Doctor of Philosophy – Mechanical Engineering

Department of Mechanical Engineering
Howard R. Hughes College of Engineering
The Graduate College

University of Nevada, Las Vegas
December 2016

UNLV | GRADUATE COLLEGE

Dissertation Approval

The Graduate College
The University of Nevada, Las Vegas

November 17, 2016

This dissertation prepared by

Srikanth Madala

entitled

Stationary Nonimaging Concentrators – A Comprehensive Study and Design Improvements

is approved in partial fulfillment of the requirements for the degree of

Doctor of Philosophy – Mechanical Engineering
Department of Mechanical Engineering

Robert F. Boehm, Ph.D.
Examination Committee Chair

Yi-Tung Chen, Ph.D.
Examination Committee Member

Woosoon Yim, Ph.D.
Examination Committee Member

Yahia Baghzouz, Ph.D.
Examination Committee Member

Rama Venkat, Ph.D.
Graduate College Faculty Representative

Kathryn Hausbeck Korgan, Ph.D.
Graduate College Interim Dean

ABSTRACT

Stationary Nonimaging Concentrators – A Comprehensive Study and Design Improvements

by

Srikanth Madala

Dr. Robert F. Boehm, Examination Committee Chair

Distinguished Professor, Department of Mechanical Engineering

University of Nevada, Las Vegas

Most places on our planet receive an annual average radiation between 800-1000 W/m^2. In the man-made world, this radiation is largely incident on stationary structures such as buildings, roads, monuments, bridges etc. Moreover, in the natural world also, there are large tracts of barren land which can be put to good use given their solar energy potential. The vision of the current research is to concentrate all this available solar energy to a more readily usable form. Therefore, stationary nonimaging solar concentrator technologies are sought after. This dissertation work is an exhaustive research on the nonimaging concentrating mechanisms with stationary applications in mind. Novel nonimaging concentrator designs have been proposed and verified through raytracing computer simulations. A possible coupling of the proposed nonimaging concentrators with passive solar tracking mechanism has also been discussed.

The effect of Fresnel reflection and total internal reflection (TIR) losses on the performance parameters and thereby, energy collection of refractive-type nonimaging solar concentrators has also been researched. A raytracing analysis has been carried out to illustrate the effects of Fresnel reflection and TIR losses on different types of stationary dielectric-filled nonimaging concentrators. The refractive index of a dielectric fill material determines the effective acceptance angle of a solid stationary nonimaging collector. Larger refractive indices yield larger acceptance angles and, thereby, larger energy collection. However, they also increase the Fresnel reflection losses. The relative benefit of increasing refractive index from an energy collection standpoint has also been assessed. This work is significant because it presents a realistic idea of the diurnal energy collection when a stationary concentrator is subjected to reflection losses. The work should be of interest to readers in the area of nonimaging optics especially when applied to stationary solar energy applications.

The application of novel design ideas to mitigate the energy losses and improve the collection efficiency has been discussed in detail. The use of anti-reflective coatings and the concept of stacked CPCs are the areas that have been explored in detail. Some truncated designs of solid nonimaging concentrators for stationary applications have also been investigated as a part of this research work. In short, this work will be found resourceful in stationary solar energy collection applications and the uses are endless, viz. building integration, stationary solar collector fields etc. Future work in the topic should investigate to solve the material constraints imposed to further improve the effectiveness of the proposed stationary solar collector designs.

ACKNOWLEDGEMENTS

The constant support I received from Dr. Robert F. Boehm, my academic advisor, is indispensable in my completion of the dissertation related research work. For this, I am ever grateful to him. He had been a constant source of inspiration to numerous students like me and shall continue to be in the future to come.

All through my doctoral journey, I had roommates who were ever-supportive and encouraging. They stood by me in my highs and lows, thus building a life-long friendship. For this, I am always indebted to them all.

My family back home in India always allowed me to pursue my passion in life. Their support and encouragement taught me to never give up on my dreams. They have always been a constant source of my strength. My cousins that live in the U.S. have been a great source of inspiration and support all through my academic career. I am thankful for their faith in me.

The Department of Mechanical Engineering has graciously supported me through a graduate teaching assistantship for the past five years which allowed me to pursue a financially unhindered education. For this, I am very thankful to them.

My advisory committee members – Dr.Yi-Tung Chen, Dr. Woosoon Yim, Dr. Yahia Baghzouz, and Dr. Rama Venkat, have been graciously supportive in my doctoral endeavors – academic and non-academic, I thank them for their support. Special thanks to Dr. Suresh Sadineni who mentored me at Center for Energy Research (UNLV) during the formative years of my doctoral journey. The College of Engineering Dean's office, GPSA, and Indian Students Association Maitri have all supported me in various academic and non-academic endeavors. UNLV library facilities have been proactive in providing the necessary academic support. I thank them all!

TABLE OF CONTENTS

LIST OF TABLES

LIST OF FIGURES

CHAPTER 1: INTRODUCTION

The Sun has been a source of energy and vitality for life on the Earth since the past four billion years. The remarkable progress achieved by a relatively new species such as the humans can be partially attributed to observing and interpreting diurnal and annual solar movements, and consequently, its effects on the surrounding environment. The human settlements leading to great civilizations would have never happened sans our knowledge of the solar movements and the causing of seasons. For the past 10,000 years, through trial and error methods or mathematical calculations, humans were always interested in tracking the Sun as their very life depended on it. Harnessing solar energy has been a primary vocation of man whether it is for agricultural needs or other daily needs. After the industrial revolution, the need for energy sources increased exponentially, leading us to high-grade energy sources such as fossil, and nuclear fuels. Solar energy which sustained us for thousands of years had been forgotten as a low-grade energy source. The early resurrection of solar energy that happened during the 19th century, with the discovery of photovoltaic effect and solar-powered steam engine, didn't gather much momentum until the early 20th century when solar energy was commercially exploited for daily needs such as domestic water heating, irrigation water pumping etc. The mid-20th century saw the invention of silicon-based photovoltaic (PV) cells, and the later part of the century witnessed PV conversion efficiency improve and prices ($\$/W_p$) drop. Nonetheless, the cheaper prices of fossil fuel alternatives have always hindered the market penetration of solar technologies through a span of more than one and half centuries now. With the dawn of new millennium, in the 21st century today, solar energy has technology on its side, improved energy collection and conversion efficiencies along with utility-scale solar power generation have made it possible to compete with the fossil fuel based energy markets. Improved energy collection and utility-scale solar thermal power generation wouldn't have been possible without the advancements in optical concentration mechanisms. Today, nonimaging optics boast of high concentration ratios in excess of 100X. Many of these high concentration systems involve precise solar tracking. However, in many cases, involving tracking systems to achieve higher energy collection is not practical either due to mechanical sophistication and/or economic feasibility.

In fact, the human zeal to accurately track the Sun's apparent motion across the sky in order to understand the intricacies of nature is not new; it existed since the dawn of human civilizations. Since the last century, with the advancement in automation and computation, there had been several technologies proposed to actively and passively track the Sun for useful concentration purposes [1]. Although tracking systems improve the collection efficiency of a solar concentrator, they also add to the capital and O&M costs while consuming a fraction of the produced power. Moreover, in certain applications such as building integration of solar technologies (viz. residential roof top PV, BiPV, solar domestic water heating systems etc.), it is a common practice to use stationary collectors because of the mechanical simplicity. Amongst the total solar electric power generated world-wide today (as per 2015 data) [2], solar photovoltaics (PV) contribute about 227 GW, and concentrating solar thermal technologies contribute about 4.8 GW. Additionally, solar energy is also used for hot water needs at a world-wide installed capacity of 435 $GW_{thermal}$. A large percentage of world's PV installations as well as solar hot water systems incorporate stationary collectors, and shall remain so in the near future. Therefore, the subject of stationary solar collectors has a renewed interest as it is a popular choice in low concentration applications.

In many applications, concentration of solar energy yields better results. Historical application of concentration can be found as early as 212 B.C. A legendary story tells us how Archimedes used bronze shields of the Greek soldiers focusing Sun's rays to burn the sails of invading Roman fleet off Syracuse. By 1st century A.D., Roman doctors were pioneers at using glass balloons filled with water to burn out wounds. Over a span of two millennia, numerous advancements happened in the field of solar optics. Both reflective and refractive solar collector designs were proposed viz. Fresnel lenses, parabolic mirrors etc. However, even the best of the traditional imaging techniques of concentration fell short of the thermodynamic limit of maximum attainable concentration ratio (CR) at least by a factor of four i.e. $CR_{imaging,\ max} \leq \frac{1}{4}\ CR_{thermodynamic,\ max}$ due to severe off-axis aberration and coma causing image blurring and broadening. Imaging is an inhibitive phenomenon as far as only concentration is concerned because the concentration of solar energy does not demand imaging qualities, but instead requires flexible concentrator designs coping with solar disk size, solar spectrum, and tracking errors while delivering a highly uniform flux [3]. It was not until 1965 that the solar energy research community has realized the redundancy of image-forming while collecting/concentrating solar energy with the discovery of 'nonimaging' type radiation collection mechanism. Nonimaging optics overcame the inherent limitations of traditional imaging optics and achieved comparatively higher concentrations. The discussion in the preceding two paragraphs set the tone for this current research which focuses on 'nonimaging' and 'stationary' techniques of concentrating solar radiation.

Nonimaging concentrators have been used in solar energy collection systems ever since their discovery in 1965. In the decades that followed, various nonimaging concentrator designs were discovered and evaluated as stationary installations. The concentration ratios achieved were typical low (<3X) or medium (3-10X). The very goal of this dissertation is to design stationary nonimaging solar energy collectors which yield better energy collection compared to the already existing designs. Various existing nonimaging concentration mechanisms such as compound parabolic concentrators (CPC), v-shaped concentrators, compound circular arc concentrators (CCAC), compound elliptical concentrators (CEC), compound hyperbolic concentrators (CHC), nonimaging Fresnel lenses etc. have all proven their superior collection efficiency over the imaging counter-parts. Moreover, the feasibility of using nonimaging concentrators successfully for stationary applications has rekindled interest in them. The economic benefits are appealing as well owing to the elimination of tracking costs (involving costs of installation, operation & maintenance, and auxiliary energy loss).

This dissertation work discusses the concept of stationary concentration, the hindrances in achieving higher concentration in stationary systems, and how to overcome the issues through design modifications. The dissertation work is classified into six chapters. The current introduction chapter familiarizes the reader of the motivation and research goals of the carried out work. The second chapter introduces the reader to the basic concepts of nonimaging concentration and the commonly used terms and definitions. A detailed literature review of nonimaging concentration systems is also presented in this chapter discussing various commonly used designs. Chapter three is an attempt to introduce the optical raytracing analysis program called ‘TracePro’ which is used extensively for the research presented in the subsequent chapters. All the simulations carried out for the current research in TracePro environment orients the designed stationary concentrators along the N-S direction. Chapter four sets into perspective the reflection losses encountered in different refractive-type nonimaging solar concentrators when used as a stationary concentrator, especially, due to the larger angles of incidence encountered. This chapter gives us an insight into how reflection losses diminish the energy collection efficiency in stationary nonimaging dielectric concentrators. Chapter five discusses various design improvements to overcome the issue of reflection losses in nonimaging dielectric concentrators whilst in a stationary application. The novel design approach of axial stacking of solid dielectric concentrators with incremental refractive indices is presented as a solution to mitigate Fresnel reflection losses. The anti-reflective coatings are another solution to diminish Fresnel reflection losses. Both of these approaches are discussed on chapter five in detail. Chapter five also quantifies the enhancement in energy collection achieved through these novel design improvements. Chapter six includes a discussion on prospective areas of application of the improved nonimaging concentrator designs, and the scope for future work to further improve the designs.

CHAPTER 2: NONIMAGING CONCENTRATION SYSTEMS

Nonimaging concentration systems are a classification of radiation collectors that direct the radiative flux passing the entry aperture (larger area, A_1) of the concentration system through to the exit aperture (smaller area, A_2) with minimum optical losses. Figure 1 shows the working principle of a nonimaging concentrator. Optical efficiency (η_{opt}) determines the optical losses (such as reflection, absorption, scattering etc.) experienced by a nonimaging concentration system. It is the ratio of the emitted radiative power, Φ_2 (in Watts) to the incident radiative power, Φ_1 (in Watts) i.e. $\eta_{opt} = \frac{\Phi_2}{\Phi_1}$. [4].

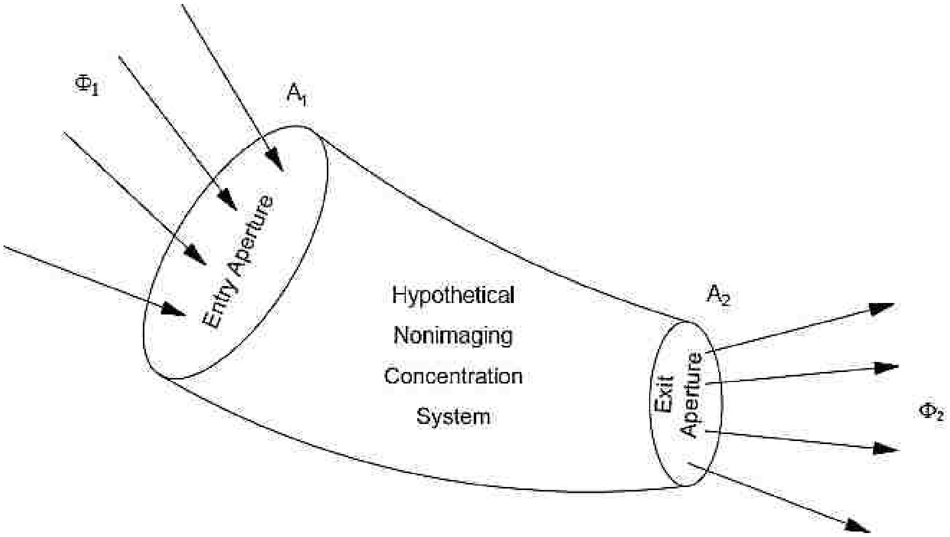

Figure 1 Nonimaging concentration system

The term ‘nonimaging’ or ‘anidolic’ (from Greek an: without; eidolon: image) refers to the feature of the concentration system to focus the étendue or ‘throughput’ on a wider area rather than a single focal point and, thus, is unable to form an image of the light source unlike the conventional imaging concentration systems. The quality of the image at the exit aperture is of least importance in these type of concentrators. Since, concentration of solar energy does not demand imaging qualities, but instead requires flexible concentrator designs coping with solar disk size, solar spectrum, and tracking errors while delivering a highly uniform flux; hence, nonimaging concentrators soon found application in solar energy collection. The difference between an imaging concentration system and a nonimaging concentration system is better explained in Figure 2. The imaging concentration system forms the images of the source points 'A' and 'B' at the receiver while the nonimaging concentration system forms no such image. However, in nonimaging concentrators, the radiative power incident on the aperture is more efficiently transferred to the receiver.

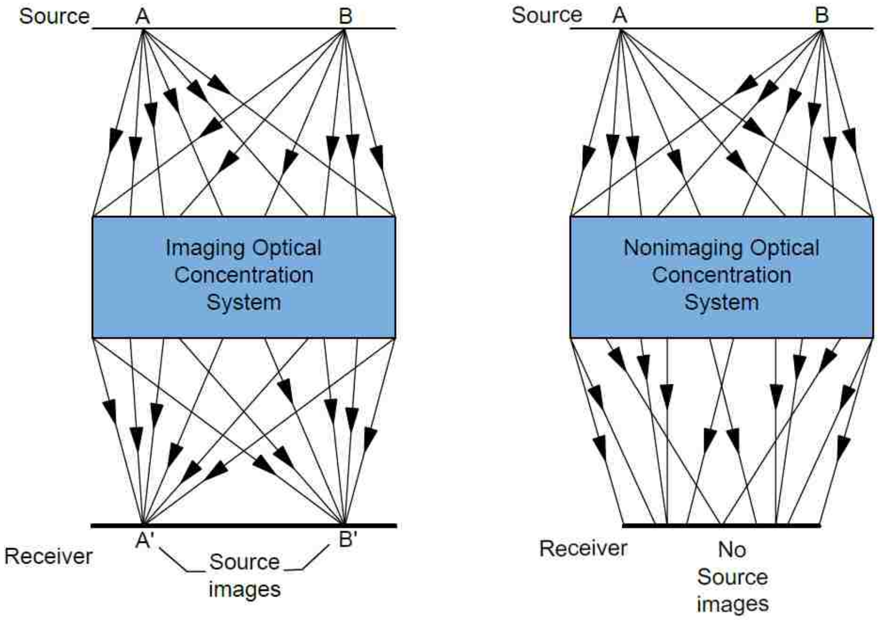

Figure 2 Comparison of imaging and nonimaging concentration systems

Typically, a nonimaging concentration system is characterized by two performance parameters – geometric concentration ratio (CR) and optical concentration ratio (CR_o). The geometric concentration ratio (CR), which is more often mentioned in the literature, is defined as the ratio of the entry aperture area (A_1) to the exit aperture area (A_2) i.e. $CR = \frac{A_1}{A_2}$. The value of CR is typically greater than 1. On the other hand, the optical concentration ratio (CR_o) is defined as the ratio of the average irradiance (I_2) integrated over the exit aperture area (A_2) to the irradiation on the entry aperture (I_1) of the collector i.e. $CR_o = \frac{\frac{1}{A_2}\int I_2 \, dA_2}{I_1}$. It can also be evaluated as a product of geometric concentration ratio (CR) and optical efficiency (η_{opt}), i.e. $\eta_{opt} \times CR = \frac{\Phi_2/A_2}{\Phi_1/A_1} = \frac{I_2}{I_1} = CR_o$ [4][5].

2.1 History, Progress and Existing Designs

The discovery of nonimaging concentration systems can be attributed to both Hinterberg and Winston when they came up with the design of compound parabolic concentrator (CPC) in an effort to measure Čerenkov radiation in a nuclear fission reactor in 1965 [4]. The following decades - the 1970s and the 1980s - saw a tremendous rise with numerous researchers experimenting on various CPC/modified CPC designs, and other nonimaging concentrator designs for solar applications [6]–[15].

The properties of various nonimaging CPC-type concentrators including the compound elliptical concentrator (CEC), compound hyperbolic concentrator (CHC), trumpet-shaped concentrator and generalized involute reflectors were discussed by Gordon and Rabl [16]. A comparative review on various reflective type solar concentrators has been reported as well [6]. Collector characteristics such as geometric concentration ratio, acceptance angle, sensitivity to mirror errors, reflector area, and average number of reflections were compared. The family of compound parabolic concentrators (CPCs) with various reflector and absorber geometries, Fresnel mirrors, V-trough concentrators and conventional imaging type concentrator designs such as parabolic trough were discussed in this review. Furthermore, two-stage concentration systems with Fresnel mirrors as a primary stage and CPC or V-trough as a secondary stage were also discussed. More recently, O'Gallagher [17] described various nonimaging collector designs in his retrospection of the research work carried out at the University of Chicago during the past 30 years. A review on solar photovoltaic concentrators briefly discussed a few designs of nonimaging concentrators such as CPC, CHC, quantum dot concentrator, dielectric total internally reflecting concentrator (DTIRC), and multi-stage concentrators [18]. Another similar review also presented a few more nonimaging concentrator designs for concentrated photovoltaic application [19]. The convex-shaped nonimaging Fresnel lens, and various other innovative multistage collector designs were discussed. The subsequent sections in this chapter describe a few prominent existing and upcoming designs of nonimaging concentrators in greater detail.

2.2 Fundamentals, Basic Concepts and Definitions

Some of the basic concepts and definitions relevant to the nonimaging concentration systems are discussed in this section.

2.2.1 Edge-Ray Principle

All the nonimaging collectors obey a fundamental principle known as the edge-ray principle (widely used in the design of nonimaging optics) which can be summed up as: “if the edge or boundary rays from a source to an optical system (reflective or refractive) are able to be directed to a target area, then all the rays in between these edge rays will be directed to the target area”. Winston et al. [20] demonstrated the edge-ray principle using the string method. The same principle has also been refined by using a topological approach [21].

2.2.2 Acceptance Half-Angle (θ_a or ψ_a)

Acceptance half-angle of a nonimaging concentrator is the angle within which the incident étendue on the entry aperture reaches the exit aperture. It is the angle subtended by the edge ray of the concentrator with the optical axis of the concentrator. When there is geometric symmetry of the concentrator along the optical axis, then the acceptance half-angle is the same on either side of the optical axis or else it will be different. Also, for a 2D-nonimaging concentrator such as a CPC trough, there will be only one pair of acceptance half-angles, however, in case of a 3D-nonimaging concentrator such as a nonimaging Fresnel lenses, there will be two pairs of acceptance half-angles – one in the cross-sectional direction and the other in the perpendicular direction.

2.2.3 Refractive Index (RI or n)

For a given wavelength (λ) of electromagnetic radiation, refractive index (RI or n) of a material is the ratio of the velocity of the electromagnetic radiation in that material medium (V) to the velocity of same wavelength electromagnetic radiation in surrounding medium (usually air or vacuum) (C), i.e. $n_\lambda = (C/V)_\lambda$. Typically for most materials, refractive index is a well-characterized material property.

However, it is a strong function of the frequency or wavelength of the interacting radiation. It also has a weaker dependency on temperature, pressure/stress, relative humidity and the composition of the material (presence of dopants etc.).

2.2.4 Sellmeier Dispersion Equation

The refractive index of a transparent material is a function of wavelength. It can be typically expressed by the equation known as Sellmeier dispersion equation as shown in (1) [4].

$$n(\lambda) = \sqrt{1 + \sum_{j=1}^{3} \frac{A_j \lambda^2}{\lambda^2 - B_j}} \tag{1}$$

Where λ is wavelength in micrometers. $A_j$and B_j are Sellmeier coefficients. These six coefficients are typically obtained from empirical data. It should also be noted that although the Sellmeier equations can be used over a wide range of wavelengths, caution is advised when applied to extreme wavelength regions (far IR and UV regions) with higher absorption.

2.2.5 Abbe Number (V_d)

Abbe number (also known as V-number) is a dimensionless number (used in optics) that is defined by the equation as shown in (2) [4]. It gives the measure of light dispersion by a material. Larger Abbe numbers correspond to lower dispersion and vice versa.

$$V_d = \frac{n_d - 1}{n_F - n_C} \tag{2}$$

Where n_d, n_F and n_C are the refractive indices of a material at blue, yellow and red lights respectively.

2.3 Design Methods and Classification of Nonimaging Concentration Systems

The very early technique of designing nonimaging optics was derived from the edge-ray principle and is known as the string method. It is highly versatile in designing 2D nonimaging concentrators (viz. CPC trough). However, its application to design of 3D nonimaging concentrators was limited. In order to address this issue, various other methods in designing a nonimaging concentrator were proposed as enumerated on

Figure 3. Among the three new methods, flow-line method is the earliest and most commonly used [20]. In recent years, the SMS method has proven its versatility in simultaneously designing two or more aspheric and freeform surfaces [22]. The freeform surfaces may not have any symmetry. The Poisson bracket method is less commonly used in the design of real world optics [23].

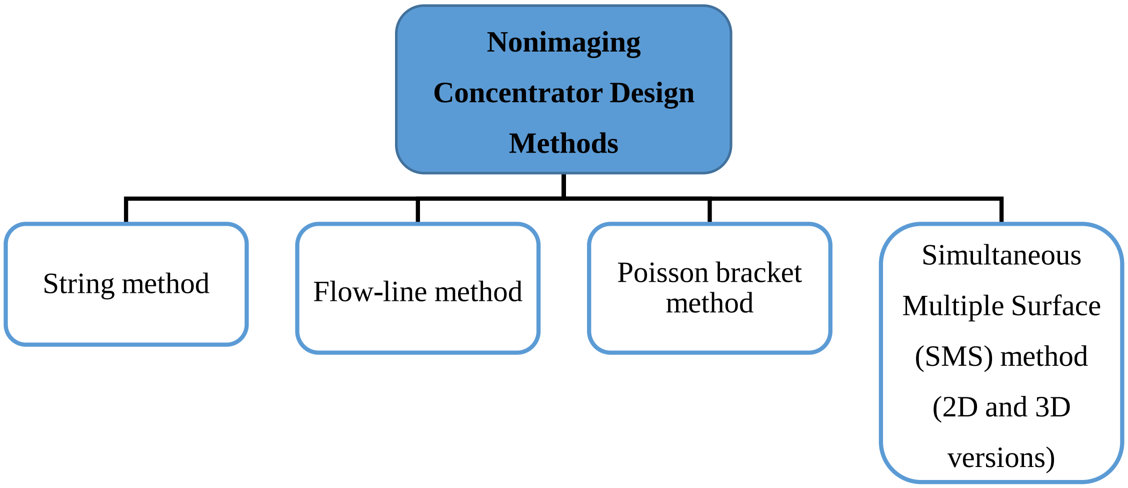

Figure 3 Different techniques used in the design of nonimaging concentrators

The nonimaging concentration systems can be classified into ideal or non-ideal categories based on the complete or partial acceptance of the incident étendue. An ideal nonimaging concentrator is characterized by distinct cut-off ranges of acceptance angles - within which all the incident radiation is completely accepted; and beyond which all the incident radiation is completely rejected. Whereas a non-ideal nonimaging concentrator experiences complete radiation acceptance within a certain range of angles and partial radiation acceptance within another range of angles. Figure 4 shows some typical examples under this binary classification of nonimaging concentrators. Among these, four commonly used designs namely – CPC, CEC, CHC and V-trough – are analyzed as a part of this dissertation research. The following sections describes these 2D nonimaging concentrator designs in detail.

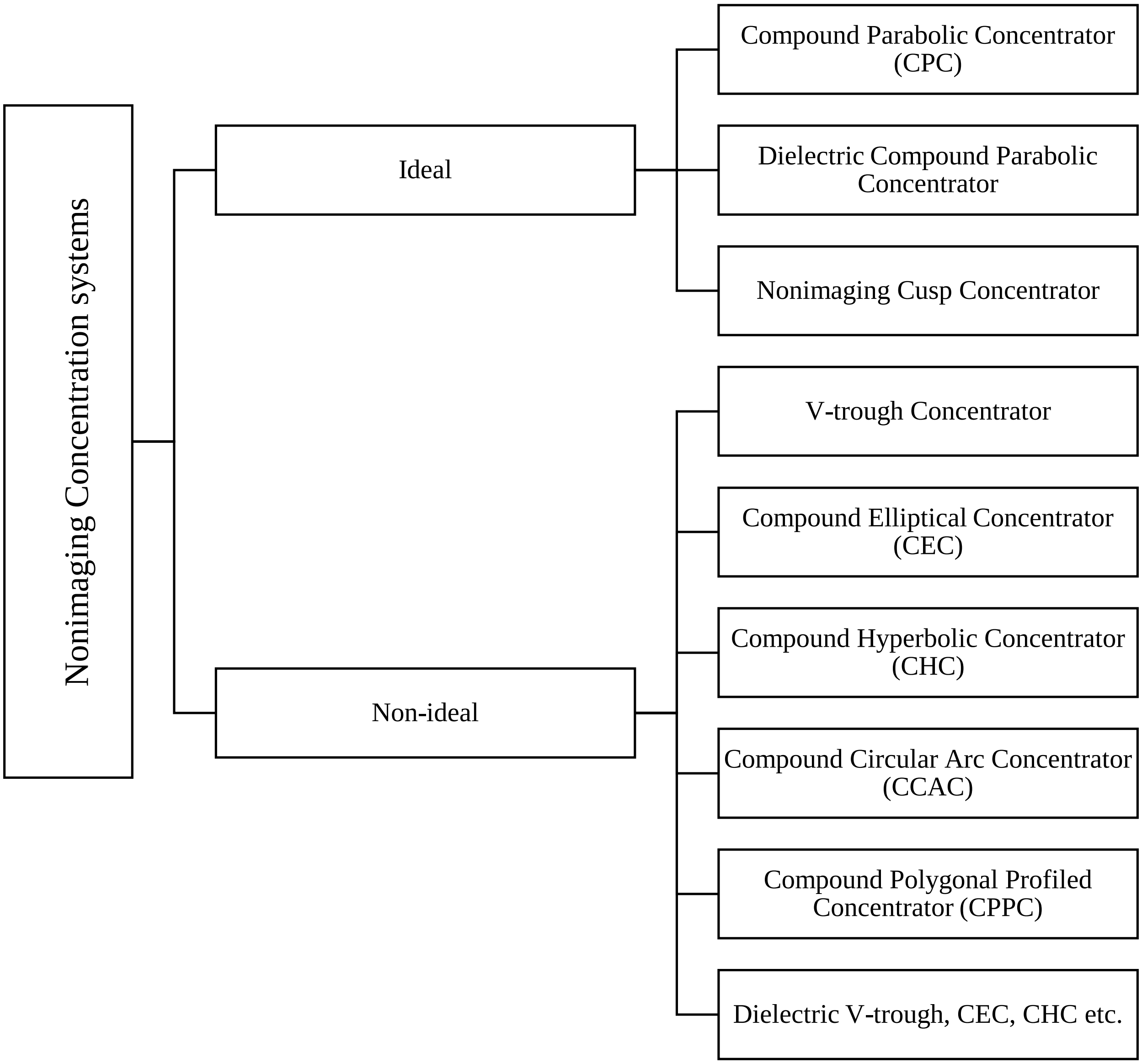

Figure 4 Classification of nonimaging concentrators

2.3.1 Compound Parabolic Concentrator (CPC)

The basic design of a CPC concentrator is as shown in Figure 5. AD and BC are two different parabolic profiles with foci at the end points of the exit aperture - B and A respectively. The tangential lines with respect to BC and AD at the end points of exit aperture - B and A - form the axes of the parabolas AD and BC respectively. The CPC attracted immediate attention of the solar energy research community with a capability of concentrating solar radiation by a factor of ~10 with just seasonal adjustment and minimal diurnal tracking [7]. For a stationary CPC, a concentration factor of ~3 is quite plausible. Also, the efficiency of accepting diffuse solar radiation enhanced further interest in their study.

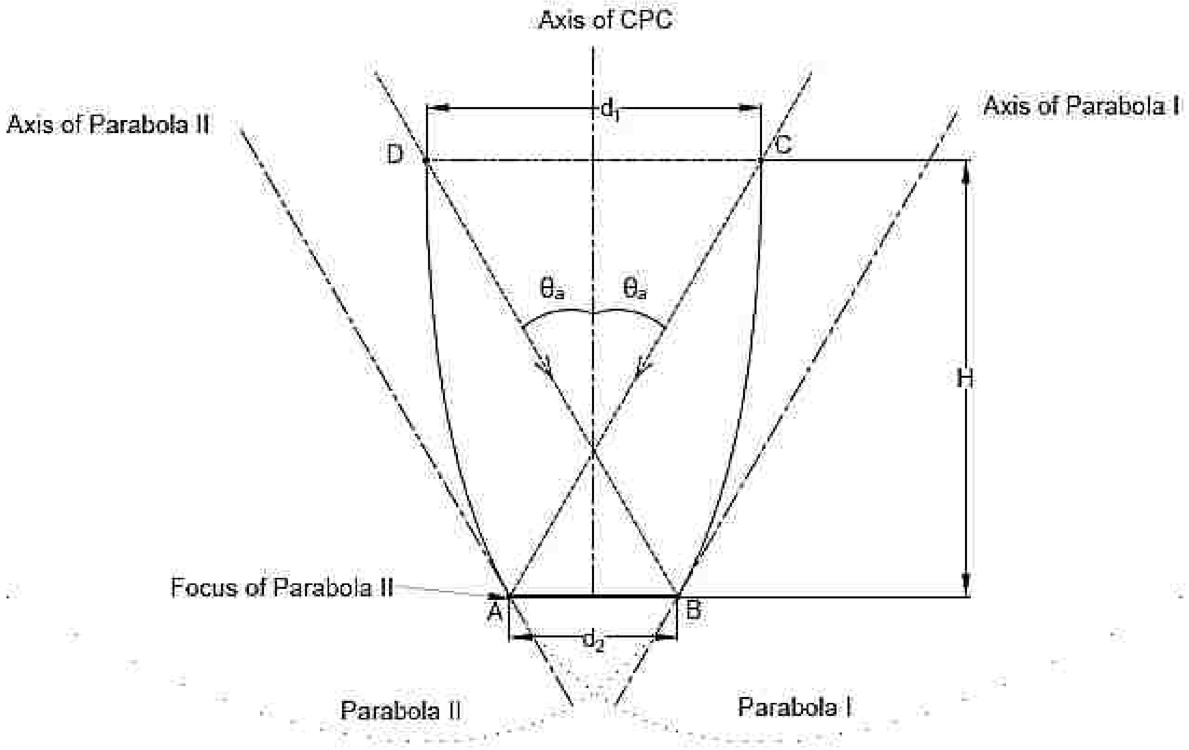

Figure 5 Compound Parabolic Concentrator

2.3.2 Compound Elliptical Concentrator (CEC)

The compound elliptical concentrator (CEC) is the design of a nonimaging concentrator where the parabolic profiles in the CPC design are replaced by elliptical profiles. In fact, CPC can be proven as a special case of CEC for an infinite source [24]. Figure 6 shows the basic geometry of a CEC in which ‘AB’ is the absorber while ‘EF’ is the radiation source. The elliptical profile - ‘BD’ is part of an ellipse whose foci are ‘E’ and ‘A’, and also passing through point ‘B’. Similarly, the elliptical profile - ‘AC’ is part of an ellipse whose foci are ‘F’ and ‘B’, and also passing through point ‘A’.

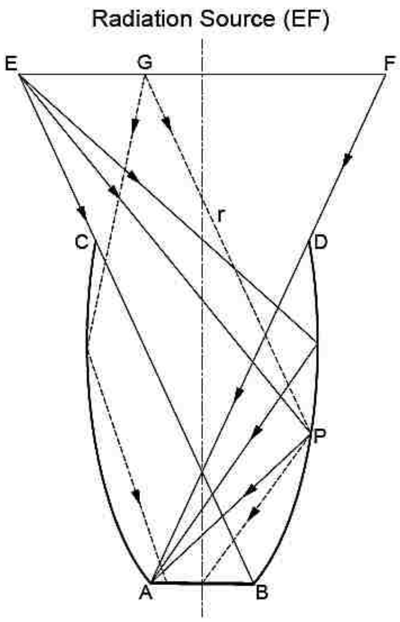

Figure 6 Compound elliptical concentrator (CEC)

2.3.3 Compound Hyperbolic Concentrator (CHC)

Compound hyperbolic concentrator (CHC) is the design of a nonimaging concentrator where the parabolic profiles in the CPC design are replaced by hyperbolic profiles as shown in Figure 7 where F1 and F2 are two foci of the hyperbola profile separated by a distance ‘2c’ with the exit aperture being ‘2a’ and the full-acceptance angle being ‘$2\theta_a$’ (which is also the asymptote separation angle) [25].

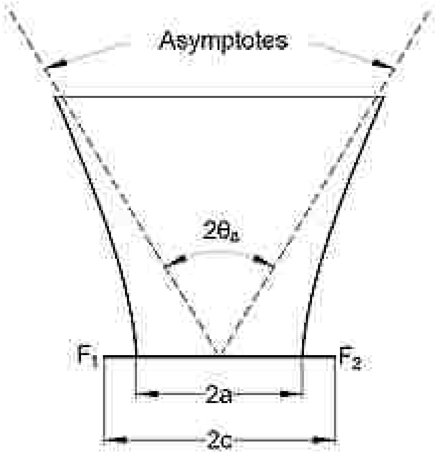

Figure 7 Compound hyperbolic concentrator (CHC)

2.3.4 V-trough Concentrator

The V-trough concentrator geometry is as shown in Figure 8. The non-hatched surface forms the reflector surface of the V-trough concentrator. Two angles – Φ (half angle of the v-shaped cone) and δ (complete acceptance angle) - play an important role in determining the amount of energy collected by a V-shaped geometry. One of the following 3 scenarios determines the complete or partial acceptance of the solar radiation by a V-trough concentrator (as shown graphically on Figure 9).

i) 100% of all the solar radiation is received within the solid angle δ will reach the absorber surface. (provided $\delta + \emptyset < {}^{\pi}/_{2}$ and $\emptyset < {}^{\pi}/_{4}$)

ii) Beyond the angle δ, there is a transition region of width $2\emptyset$ with center at $\delta + \emptyset$. In this transition region, only part of the received radiation is transmitted to the absorber surface.

iii) Any radiation beyond the maximum acceptance angle ($\theta_c = \delta + 2\emptyset$) is rejected and will never reach the absorber surface.

The geometric concentration ratio for these types of concentrators is given by equation (3).

$$CR_{v-trough} = \frac{1}{\sin(\delta + \emptyset)} \tag{3}$$

Previous research has proven that the higher the concentration, the greater is the relative advantage of CPC over the V-trough geometry [6]. At a geometric concentration ratio of 3, the hollow V-trough design seems almost impractical. A quantitative comparison between V-trough and CPC is difficult because of the large number of parameters that should be considered simultaneously. Even disregarding reflector cost and solar energy collection, the comparison involves additional parameters (ratio of reflector to aperture area, number of reflections, acceptance angle and truncation) besides the value of just geometric concentration ratio. The recent material developments lead to improved reflective surfaces which may improve the overall year round energy collection efficiency of a nonimaging concentrator with V-trough profile compared to compound parabolic profile in low (<3X) and medium (<10X) concentration applications.

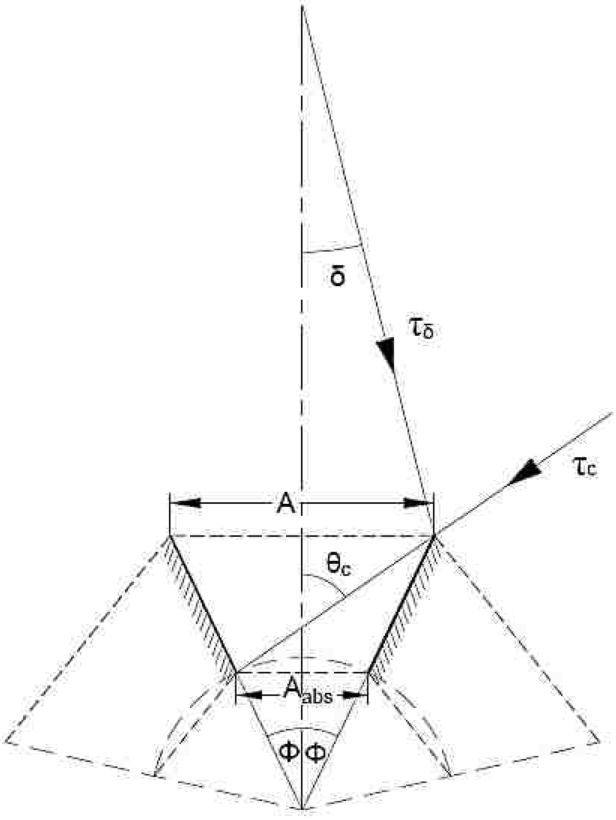

Figure 8 V-trough concentrator with mirror images and reference circle. The rays τ_δ and τ_c, have angle of incidence δ and θ_c, respectively; they pass through the edge of the absorber and are tangential to the reference circle

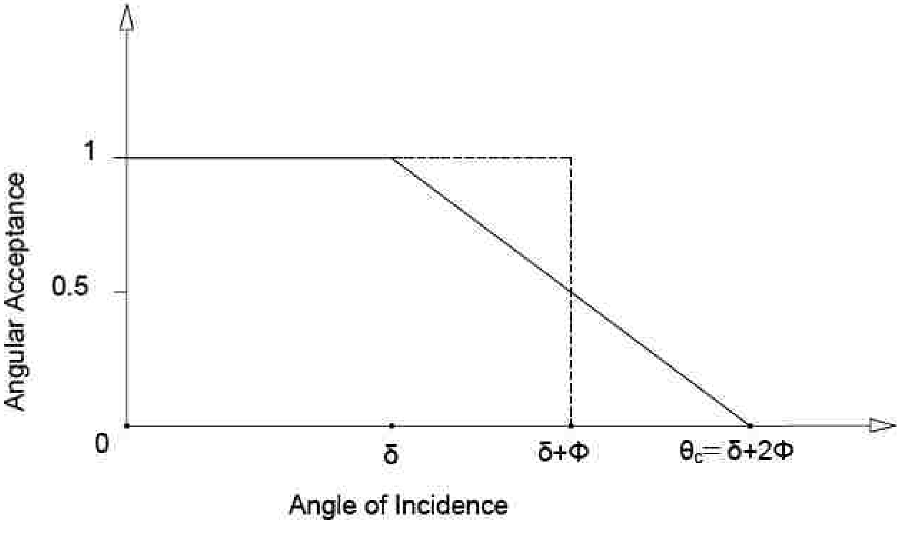

Figure 9 Angular acceptance of V-trough varying with the angle of incidence

2.4 Optical Modeling Using Computer Programs

The field of optical modeling has seen tremendous progress in the past two decades due to the exponential increase in computing power. Early optical modeling efforts on CPCs involved using multiple programs to achieve the desired ray-tracing results. Viz. AutoCAD was used in conjunction with LOTUS 1-2-3 and FORTRAN to model and ray-trace a cusp-type CPC with cylindrical absorber [26].

Currently, there are commercially available optical modeling software that can be handy in optical modeling of various designs. These programs can be broadly classified into 3 categories: sequential ray-tracing type, non-sequential ray-tracing type and finite-difference time-domain (FDTD) simulation type. Sequential ray-tracing software interacts with the light from a user-defined source in a sequentially defined manner. Each surface in the optical system interacts with the light one at a time in the order defined by the user. These type of programs are typically used to model optical systems such as cameras, endoscopes, microscopes, telescopes etc. Examples of such programs are CODE V, ASAP etc. On the other hand, non-sequential programs allow the ray interaction with any surface multiple times without any predetermined sequence. Ray-scattering and Fresnel reflections are effectively accounted for, leading to more accurate modeling of real world interactions. Some non-sequential optical modeling programs can also model coherent systems through the Gaussian beam summation method. These type of programs are typically used to model imaging systems, light pipes, backlights, luminaires etc. Examples of such programs are Optics Lab, ZEMAX, OSLO, TracePro, FRED, Light Tools etc. When the size of the optical system shrinks to the wavelength-scale, the Gaussian beam summation modeling breaks down. That is when FDTD programs come in handy. They solve for Maxwell’s equations to propagate electro-magnetic fields through micro and nano-scale optical systems. Examples of such programs are Virtual Lab, SPEOS etc. [27]

Optical simulation software such as TracePro, OptiCAD and ASAP had been reportedly used to simulate the performance of nonimaging Fresnel lens or nonimaging optics in general [28][29]. Optimization algorithms are frequently embedded in these types of software to perform design optimization of a newer design. OptiCAD was used to compare the optical performance of a linear Fresnel lens (10X concentration), and a hybrid system of linear Fresnel (5X concentration) + CPC (2X concentration) [28]. This 3D analysis showed the effect of transverse and longitudinal angles on focus and the optical concentration ratio. The hybrid system of 5X linear Fresnel lens + 2X CPC proved more effective for stationary applications (BIPV in this case).

CHAPTER 3: OPTICAL ANALYSIS USING TRACEPRO

The optical analysis work all through this dissertation research is carried out with the help of a raytracing computer program known as TracePro Expert 7.8.0. It is an illumination design, analysis and optimization software created by Lambda Research Corporation.

3.1 Introduction to TracePro

The discussion that follows will describe a few key features of the TracePro opto-mechanical modeling software. Those features of the program that are only relevant to this dissertation work are described here. An exhaustive detail of the program can be obtained from the TracePro user's manual published by Lambda Research Corporation [30].

3.1.1 Menu bar and Toolbars

The menu bar and the toolbars in TracePro provide access to the required tools in all stages of the raytracing analysis – designing a solid model (menu item → Geometry), applying the required opto-mechanical properties (menu item → Define), defining the light sources (menu item → Define), carrying out the raytracing analysis (menu item → Raytrace), and finally analyzing the raytracing results (menu item → Analysis, and Reports). Additional menu items – Optimize, Tools, Utilities and Macros further improve the versatility of the program. A screenshot comprising both the menu bar and the toolbars is shown on Figure 10.

Figure 10 TracePro Menu bar (items) and Toolbars (icons)

3.1.2 Model Window

TracePro uses an ACIS-based geometry engine where in the solid model data is stored as an ACIS database file. The file extension is .SAT for ACIS files. Figure 11 shows the model window in TracePro and is reminiscent of any ACIS-based solid modeling environment such as SolidWorks etc. All the solid models built or imported to TracePro are displayed in this space. Also, the model window has a display of the light sources defined within the program as well. The TracePro file that includes the solid model and the light sources is saved with .OML file extension. The information regarding the solid model's surface and material properties, and the light sources' geometry, spatial location and spectral distribution are all part of the saved OML file. The model tree and the source tree that are discussed in the following sections are part of the saved OML file.

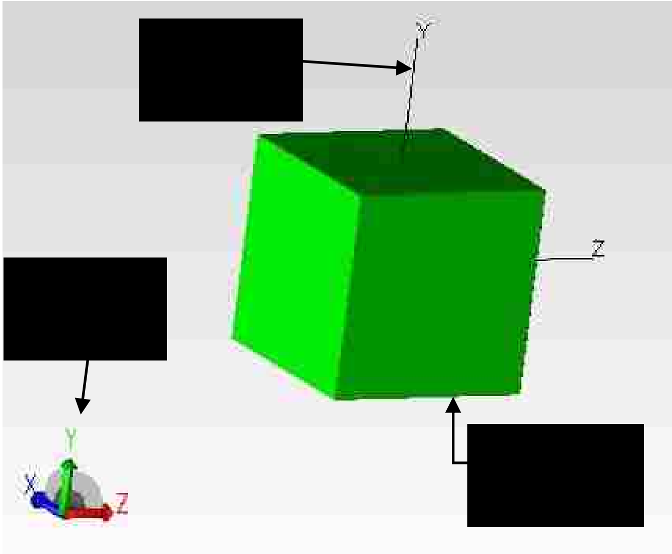

Figure 11 TracePro Model Window

3.1.3 Model Tree

The solid model represented on the model window is supplemented by a model tree that is shown on Figure 12. All the surfaces of the representative solid geometry are shown here. In this graphical user interface, the plus and minus controls are used to expand and collapse the opto-mechanical property details of a respective surface or an object. It should be noted that the 'Model' tab is active on the system tree in Figure 12 in order to access the model tree. All the optically active objects are indicated by a preceding green check (✓), and the inactive objects by a red cross (×).

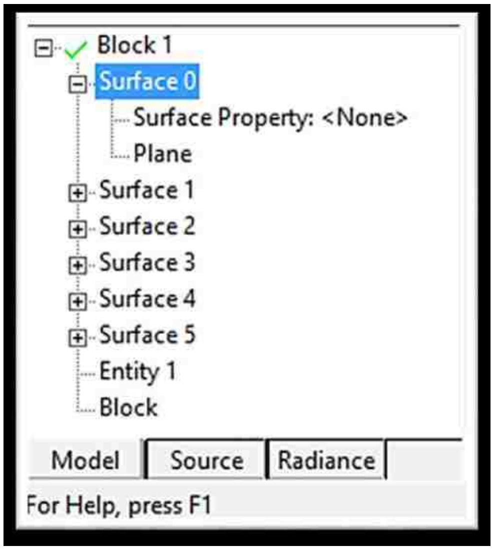

Figure 12 System Tree of the solid model (‘Model’ tab is active)

3.1.4 Source Tree

As shown in Figure 13, three different types of light sources can be defined in TracePro - Grid, Surface and File sources. A grid source is a rectangular or circular in shape light source with a chosen density of rays emanating with a user-defined spatial and spectral distribution. During the course of this research, rectangular grid sources were designed corresponding to the size of the entry aperture and simulated. However, TracePro also allows the user to designate a particular surface of a solid geometry as a light source i.e. a surface source, or import a ray file i.e. a file source. All the active sources are indicated by a preceding green check (✓), and the inactive sources by a red cross (×) on the source tree as well.

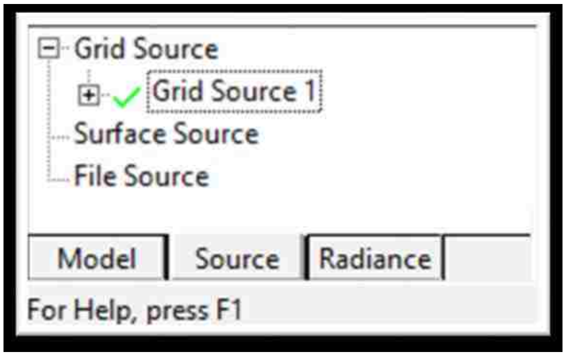

Figure 13 Source Tree (‘Source’ tab is active)

3.1.5 2D Interactive Optimizer in TracePro

The 2D interactive optimizer is a utility on TracePro that can be found under the ‘Optimize’ menu bar item of the TracePro program. This tool is very useful in creating and optimizing two-dimensional shapes. The menu bar on the 2D interactive optimizer is different from TracePro’s original menu bar and is as shown on Figure 14. It also shows the toolbox in the 2D interactive optimizer interface that can be used to model the interactive 2D geometries which will eventually be exported to TracePro model window interface as a rotational or translational 3D geometry. The property editor (refer to Figure 15) is used to make changes to the interactive 2D geometry as well as apply surface properties to the selected curve. The interactive 2D geometry window displays the geometry and is as shown in Figure 16. Any of the points, lines and curves can be selected and modified in this graphical user interface. The rotational axis can be modified from the selection below the menu bar to suit the needs of the user. Another key feature of the 2D interactive optimizer is that it also uses downhill simplex method to optimize the geometry if opted by the user.

Figure 14 Menu bar and Toolbox in 2D-interactive optimizer utility

Figure 15 Property Editor in 2D-interactive optimizer utility

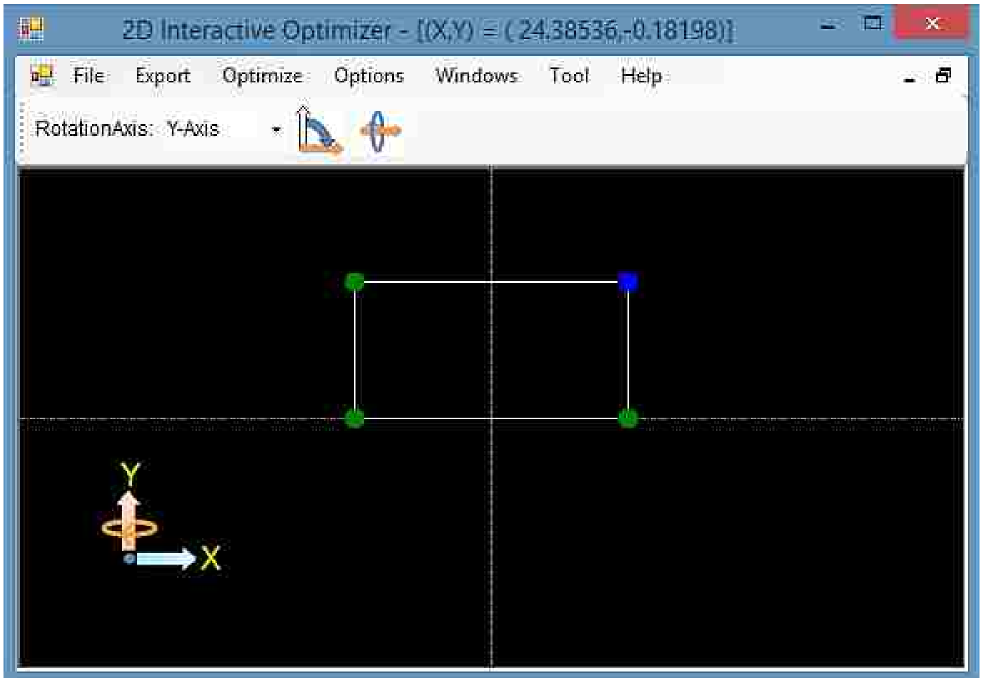

Figure 16 Interactive sketch window in 2D-interactive optimizer utility

3.2 Workflow in TracePro

The general workflow in TracePro program is as presented on Figure 17. In the first step, a 3D solid geometry is created using the available modeling tools on the toolbars and/or menu bar. Various primitive solid shapes including blocks, cylinders and cones, spheres, tori, and thin sheets are available to aid in the creation of a solid model. Also, commonly used objects that comprise an opto-mechanical system such as lens element, Fresnel lens, reflector, tube or baffle vane are readily available in TracePro. Boolean logical operators – intersect, subtract, and unite are available to mold complex geometric shapes from primitive ones. Sweep and revolve commands are used to further modify the created solid object. The choice of physical units can be altered under the 'preferences' section. By default, the dimensions are in millimeters.

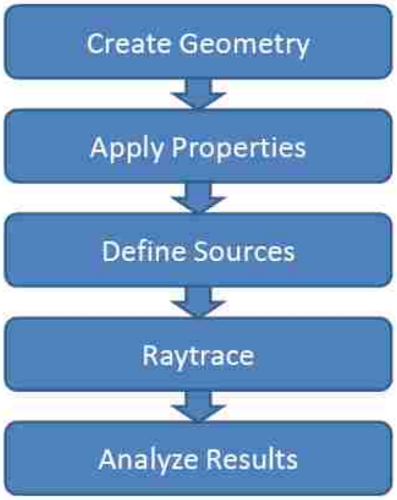

Figure 17 Schematic of workflow in TracePro

Applying opto-mechanical properties is the second step in the workflow after the creation of a solid geometry. These properties determine how the rays interact with a given surface or object. The 'Apply properties' category can be broadly classified into physical, raytrace and other properties. Table 1 shows further classification of these properties that can be modified. TracePro provides the user with a built-in exhaustive database of the opto-mechanical properties of commonly available material [30]. Any of these properties can be selected from the existing database, or can be user-defined as well.

Defining radiation sources is the third step in the workflow before carrying out the raytrace. The radiation sources are defined as one of the three available source types – grid, surface and file. A grid source is defined as a virtual window to a distant source with rays emanating from that window. A surface source is applied as a property of a chosen surface. A file source is defined as ray data file that can be processed by TracePro. A raytrace simulation can include radiation flux from multiple sources which can be a combination of any of the aforementioned radiation source types.

Table 1 TracePro ‘Apply Properties’ categories.

	Object	**Surface**
Physical Properties	Material Temperature Mueller Matrix (polarization) Gradient Index Bulk Scattering	Surface Surface Source Diffraction Temperature Temperature Distribution RepTile
Raytrace Properties	Raytrace Flag Importance Sampling	Surface Source Prescription Importance Sampling Exit Surface
Other Properties	Color Class and User Data	Color

The fourth step of raytracing analysis is carried out either in ‘analysis mode’ if the interaction with all the objects is desired, or in ‘simulation mode’ if interaction with only certain surfaces is desired. The raytrace options can be edited before carrying out the raytracing analysis. The important options that can be edited includes analysis units (radiometric or photometric), ray splitting, importance sampling, aperture diffraction, random rays, fluorescence, and polarization. The flux thresholds can also be adjusted to a desired value. Also, the type of voxelization (Voxels are 3D pixels) and the maximum voxel count determines the raytrace speed and memory consumption.

The final step is to analyze the raytracing results. This can be performed in various ways. Irradiance and illuminance maps (in 2D and 3D) and candela plots are ways to graphically visualize the raytrace results. All the ray histories and incident ray information will also be available on TracePro. The flux report will have detailed information regarding the amount of energy (in Watts) incident on each surface.

3.3 Alternative Workflows in TracePro

The workflow in TracePro can be alternatively modified to match one of the three types of workflow shown on Figure 18. In the first alternative workflow, the creation of a solid geometry can be carried out in another CAD Program (with ACIS interface) and imported to TracePro, and continue with the rest of the workflow as shown on Figure 18A. Besides the ACIS files, TracePro is also compatible with CAD translators such as IGES, Inventor, Pro/E, STEP, HOOPS Stream and HOOPS metafile. Furthermore, it is also compatible with popular lens design applications such as CodeV, OSLO and ZEMAX.

The second alternative workflow suggests the use of an additional add-on to TracePro called the TracePro Bridge for SolidWorks which eliminates the steps of creating the geometry, applying the opto-mechanical properties, and defining the light sources. Both the geometry and light sources are created in SolidWorks environment and imported to TracePro. Then the raytracing computation and analysis of results are performed in the TracePro program. Figure 18B depicts this type of workflow.

The third alternative workflow is illustrated on Figure 18C. Instead of creating the solid model in the model window, the TracePro's built-in 2D and 3D interactive optimizers can be alternatively used to create the solid model which can later be imported to the model window for carrying out the rest of the workflow as indicated on Figure 18C.

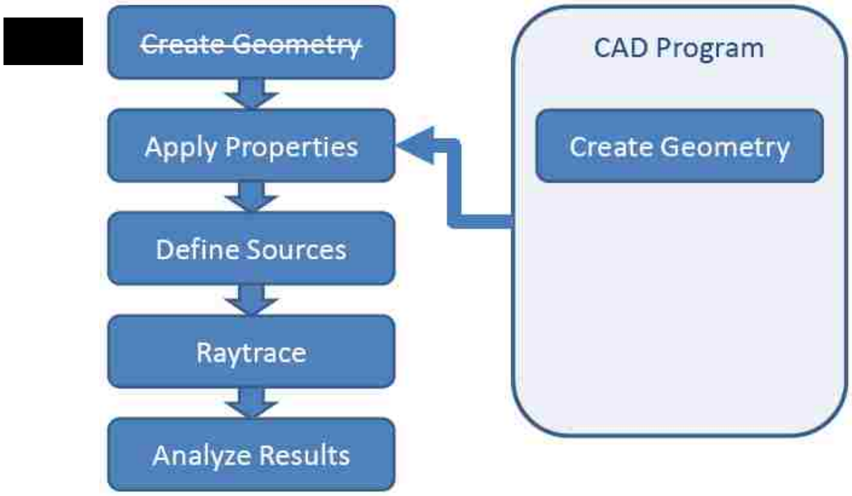
[redacted]

[redacted]

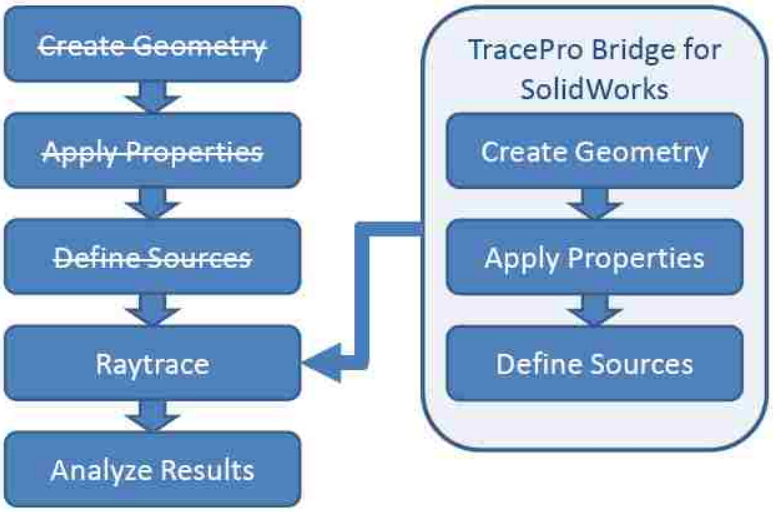

(C)

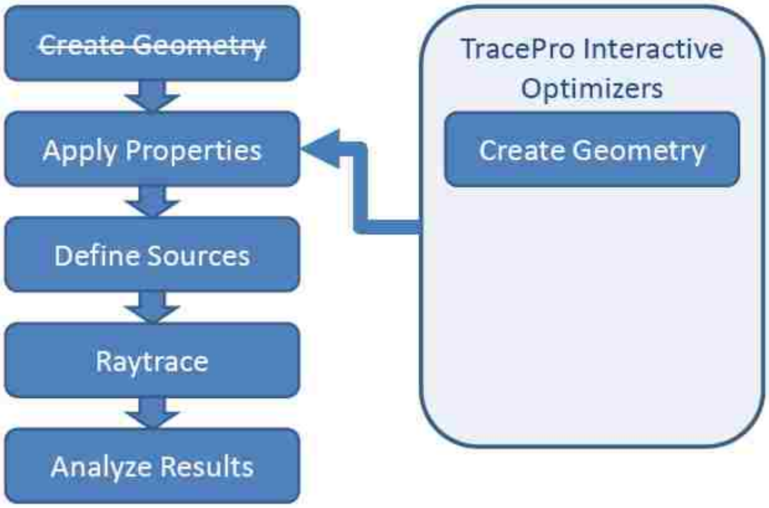

Figure 18 Three different types of alternate workflows in TracePro

CHAPTER 4: REFLECTION LOSSES IN DIELECTRIC NONIMAGING CONCENTRATORS

Traditionally, a dual-axis solar tracking mechanism was involved in refractive-type imaging solar concentrators such as conventional lenses, Fresnel lenses etc. as achieving paraxial incidence is vital for image forming, and thereby improved energy collection at the absorber surface. However, in the recent decades, with the discovery of nonimaging solar concentrators, it had been proven that image-forming is not a necessary condition for achieving higher concentrations. A nonimaging concentrator is characterized by its acceptance angle within which it completely or partially accepts all the incident radiation. A solid nonimaging concentrator is typically filled with a dielectric material which has a refractive index greater than air (i.e. RI>1) allowing it to accept more étendue compared to its hollow counterpart. It is intriguing to explore the potential of these refractive-type nonimaging concentrators for stationary applications. In the case of refractive-type ‘imaging’ concentrators, Fresnel reflection and total internal reflection (TIR) losses were barely a topic of analysis because the incident paraxial radiation encountered minimum Fresnel reflection loss at the entry aperture and almost no total internal reflection (TIR) loss inside the optic. But, that is not the case with stationary refractive-type nonimaging concentrators. Since, the radiation is non-paraxial at most incidence angles, the effect of Fresnel reflection and total internal reflection (TIR) losses become a topic of discussion.

Increased refractive index of dielectric fill material means higher effective acceptance angle by the nonimaging concentrator i.e. higher energy collection at the absorber. However, it also means, higher Fresnel reflection losses at the entry aperture. This chapter discusses the effect of refractive index on reflection losses (both Fresnel reflection and total internal reflection losses) as well as energy collection improvement in stationary dielectric-filled nonimaging solar concentrators. Increment of refractive index is a double-edged sword, although it increases the acceptance angle and thereby the energy collection by the concentrator, it also results in increased Fresnel reflection losses at the entry aperture. An optimum refractive index value is calculated for four different stationary nonimaging concentrator designs through raytracing evaluations.

4.1 Fresnel Reflection Phenomenon

According to the Fresnel equations [31][32], when light traverses an interface between two homogenous, isotropic, non-magnetic, dielectric media of different refractive indices, both refraction and reflection may occur at the interface. The associated reflection at the interface is known as Fresnel reflection. Figure 19 is an illustration of the Fresnel reflection phenomenon at the air-dielectric interface.

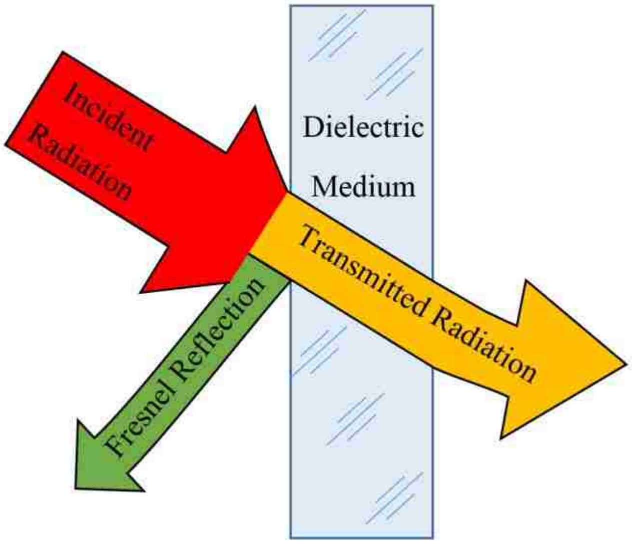

Figure 19 Fresnel reflection phenomenon at the interface of a dielectric medium

It is predominantly influenced by the refractive index of the dielectric medium and the angle of incidence at the interface; while the spectral effect on Fresnel reflection is negligibly small. For instance, at an air-PMMA interface, the variation of reflectance (ratio of the reflected flux to the incident flux) and transmittance (ratio of the transmitted flux to the incident flux) with respect to the angle of incidence are as shown in Figure 20. The governing Fresnel equations are discussed in Appendix I. Also, from Figure 21, we can notice that the average transmittance (T_{avg}) of the material, after the Fresnel reflection at the air-material interface (entry aperture), is almost constant until 50° angle of incidence; beyond which the transmittance drops exponentially due to higher Fresnel reflection.

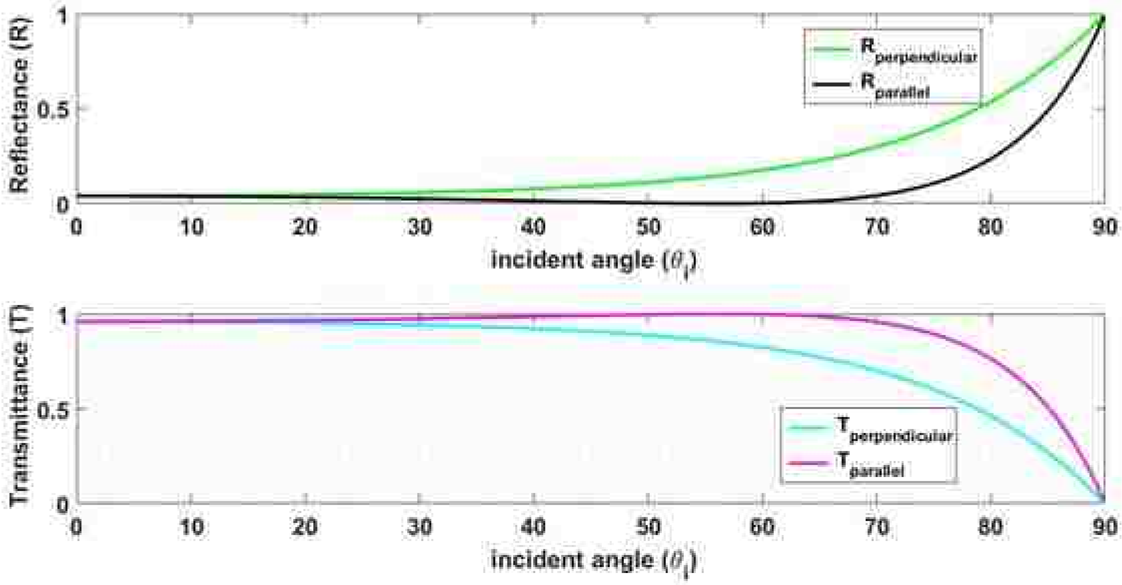

Figure 20 Variation of transmittance (T) and reflectance (R) as a function of incident angle and the refractive indices of the dielectric media (air, n_1=1 and PMMA, n_2=1.4805-1.5050). The suffix indicates the type of polarization – parallel and perpendicular. Also, note that T+R=1 in both cases

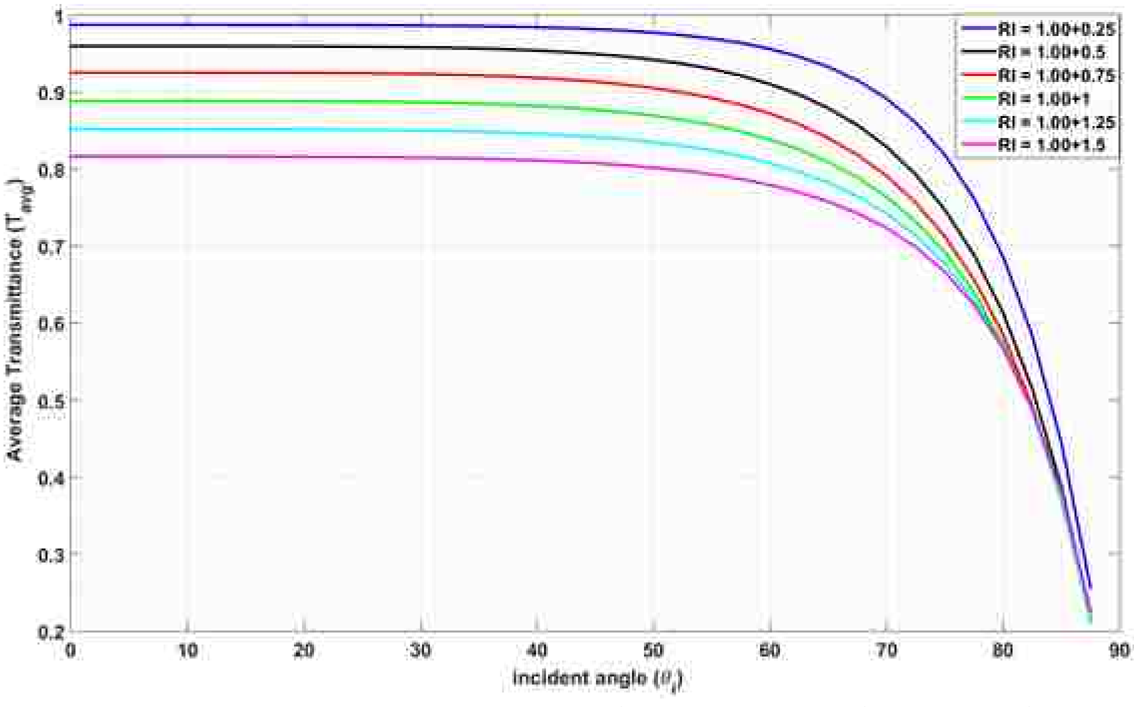

Figure 21 Average Transmittance [$T_{avg}=(T_{\perp}+T_{\parallel})/2$] of incident radiation after Fresnel reflection by different refractive index materials (RI=1.25, 1.5, 1.75, 2, 2.25 and 2.5)

As shown in Figure 21, the trend of the effect of Fresnel reflection loss on transmittance is all the same to materials with different refractive indices. Also, as the refractive index value increases, so does the Fresnel reflection loss which eventually decreases the average transmittance. Viz. the average transmittance for a refractive index of 1.25 is around 0.987 for angles of incidence within the range of [-50°, 50°]. Whereas for a refractive index of 2.5, the value of transmittance is around 0.816 within the same range of angles of incidence.

4.2 Effect of Reflection Losses on a Dielectric-Filled Solid Nonimaging Concentrator

Reflection losses (both Fresnel reflection loss and TIR reflection loss due to contour shape) play an important role in determining the performance parameters of a stationary dielectric-filled solid nonimaging solar concentrator. Four different stationary nonimaging concentrator geometries - a dielectric-filled solid V-trough, CPC, CEC and CHC (all of the same geometric concentration ratio, CR=2.25 and PMMA as dielectric fill material, RI=1.4805-1.5050) are modeled in the TracePro raytracing software as shown in Figure 22. The entry aperture of all the four geometries is maintained at 4.5×100 mm while the exit aperture or absorber dimension is maintained at 2×100 mm. All the concentrators individually interact with the same 71 sources of radiation modeled in the TracePro program as well. Each of the radiation sources are spaced at 2.5° solar azimuth angle apart in the range of [-87.5°, 87.5°] while the solar altitude angle is maintained at 0°. The sources are modeled such that they emit a solar flux that is varying hourly based on National Renewable Energy Laboratory's (NREL) TMY3 data [33] (723860 – Las Vegas McCarran Intl AP) for 183rd Julian day (corresponding to July 1st). All the four concentrators are aligned with their horizontal axes in the N-S direction. All throughout, a reference solar spectral irradiance (for wavelengths between 0.28 and 4.0 µm) as defined by ASTM G173-03 standard [34] is being simulated. This work closely simulates performance of all the four nonimaging solar concentrators on a typical summer day in Las Vegas, NV. The attenuation coefficients of PMMA and other theoretical material used in the simulation are assumed to be negligible, so the only losses encountered are the reflective losses. The simulation results are quantified as performance parameters – concentration ratio (CR), optical efficiency (η_{opt}), optical concentration ratio (CR_o) and total diurnal energy collection in the following sections.

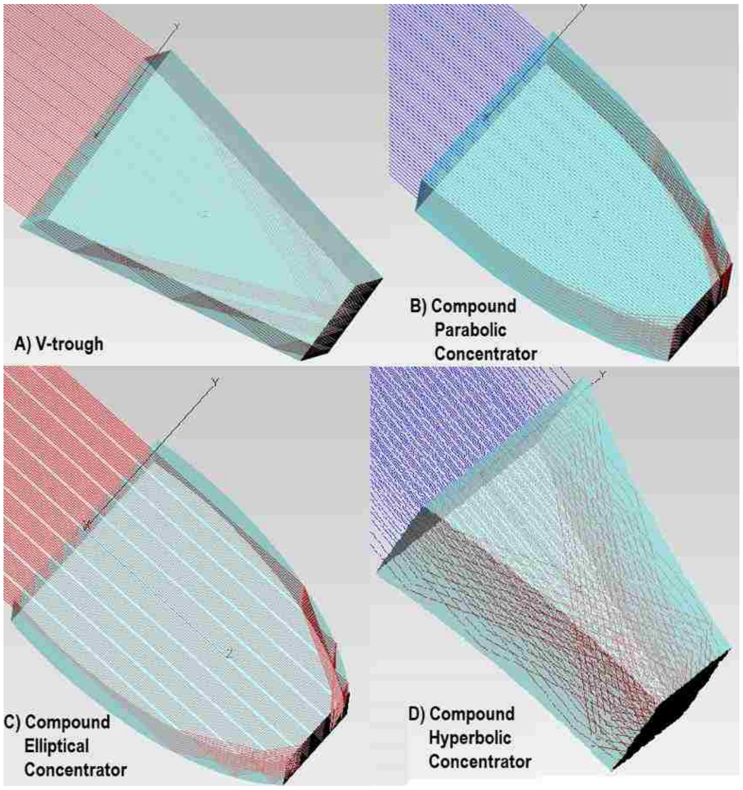

Figure 22 Dielectric-filled solid nonimaging solar concentrators

4.2.1 Fresnel Reflection Losses

The reflection losses occurring at the entry aperture (air-dielectric interface) of the nonimaging optic are characterized as Fresnel reflection losses. The magnitude of Fresnel reflection loss is determined by the refractive index (RI) value of the optic material and the angle of incidence (θ_i). Figure 23 shows the amount of radiation lost due to Fresnel reflection for different dielectric material of varying refractive indices. A noticeable change in Fresnel reflectance is observed for angles of incidence beyond the range of [-50°, 50°]. Within the range of [-70°, -50°] ∪ [50°, 70°], the increase in Fresnel reflectance is gradual. Furthermore, beyond the angle of incidence range of [-70°, 70°], the Fresnel reflectance increases exponentially and, thus, dominates the reflection losses. Also, it should be noted that the spectral (wavelength) effect on

Fresnel reflection is negligibly small compared to the angular effect and, thus, an average effect over the solar spectrum (0.28 - 4.0 µm) is evaluated as per the equations discussed in Appendix A.

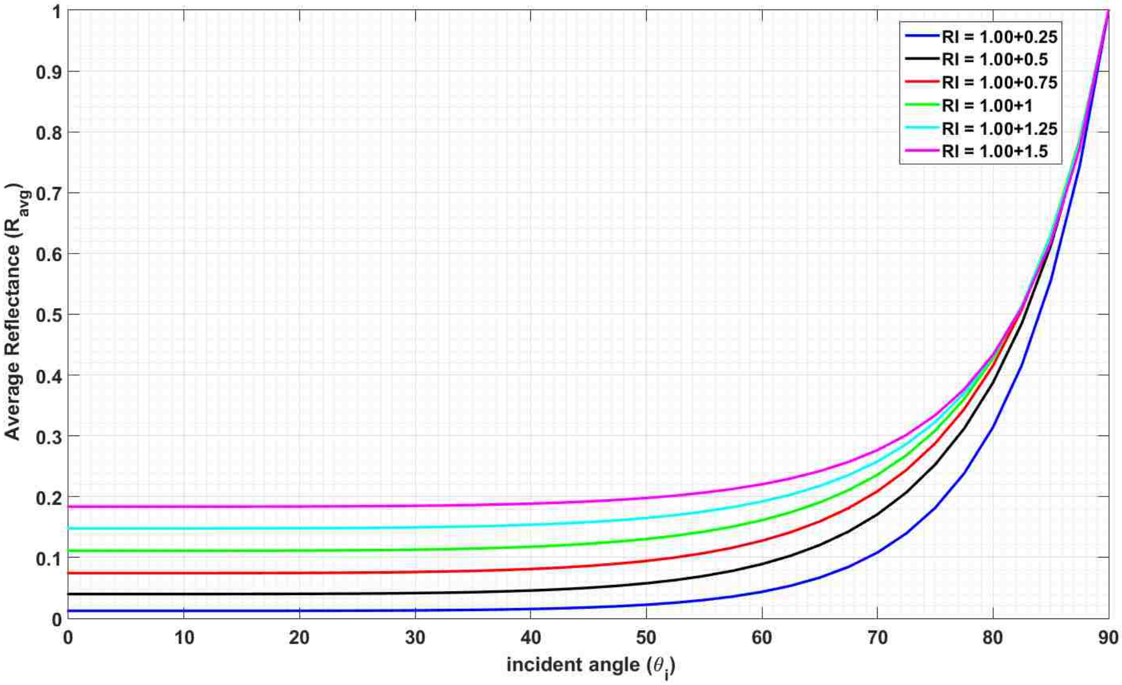

Figure 23 Average reflectance [$R_{avg}=(R_{\perp}+R_{\parallel})/2$] of incident radiation after Fresnel reflection by different refractive index materials (RI=1.25, 1.5, 1.75, 2, 2.25 and 2.5)

4.2.2 Total Internal Reflection (TIR) Loss Due to Shape of the Reflector Contour

Besides the Fresnel reflection loss, there is another prominent reflection loss encountered in the stationary dielectric-filled non-imaging solar concentrators, i.e. the total internal reflection (TIR) loss. In fact, the total internal reflection phenomenon causes the reflector walls to direct the radiation on to the absorber surface. However, the same phenomenon and shape of the wall contour in combined effect are also responsible for reflecting back some part of the étendue that is incident beyond the effective acceptance angle range. The TIR loss is the secondary contribution factor to the reflection losses as only that portion of the radiation that survives the Fresnel reflection loss at the entry aperture will encounter TIR inside the nonimaging optic. The magnitude of the TIR losses due to the shape of the reflector wall contour for all the four simulated nonimaging concentrators are shown on Figure 24**.** On the y-axis, only the TIR type of reflection losses are shown. For an ideal nonimaging concentrator such as CPC, the TIR losses are non-existent within the range of acceptance angle ([-40°, 40°] in this case). All the incident radiation surviving Fresnel reflection within that range will reach the absorber. For other nonimaging concentrators – CEC, CHC and V-trough – the TIR losses steadily increase beyond a certain angle and increases until 70°, after which the Fresnel reflection losses are comparatively dominant and take over.

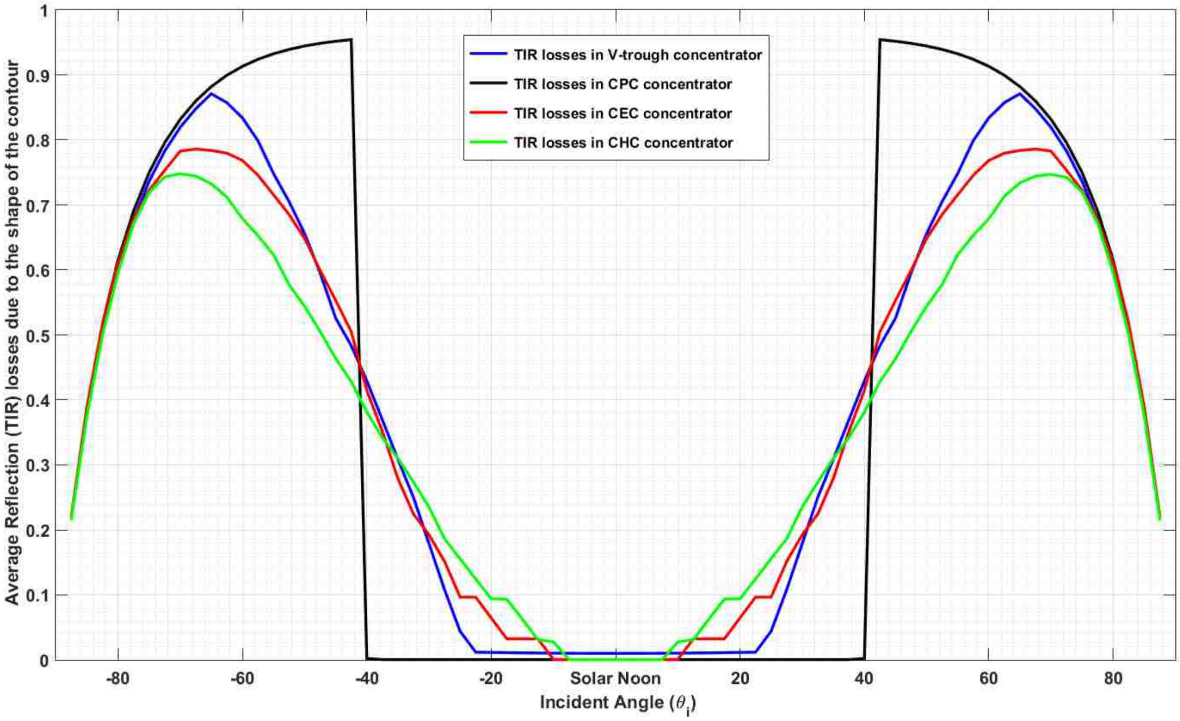

Figure 24 Total internal reflection losses due to the contour shape of the nonimaging concentrator

(Solid fill material – PMMA, RI = 1.4805-1.5050)

4.3 Comparison with Hollow Counterparts

A comparative analysis of the four considered solid geometries – V-trough, CPC, CEC and CHC – with their respective hollow counterparts has also been carried out. Figure 25 illustrates all the hollow geometries that are modeled on TracePro raytracing computer program. The total diurnal energy harvested (in kWh/m^2-day) by the four stationary nonimaging solid concentrators and their hollow geometry counterparts during the period of a typical summer day (July 1st) in Las Vegas, NV is evaluated and are shown on Table 2. Also shown on Table 2 is the diurnal average optical efficiency (η_{opt}) of all these concentrator geometries. Furthermore, the product of geometric concentration ratio (CR=2.25) and optical efficiency (η_{opt}) is shown as optical concentration ratio (CR_o) in the same table as well. The significance of a solid dielectric fill in improving the energy collection is conspicuous with all the presented data comparing solid and hollow geometries on Table 2. The total diurnal energy collected by a stationary solid dielectric fill concentrators is about 41-43% more than their respective hollow counterparts.

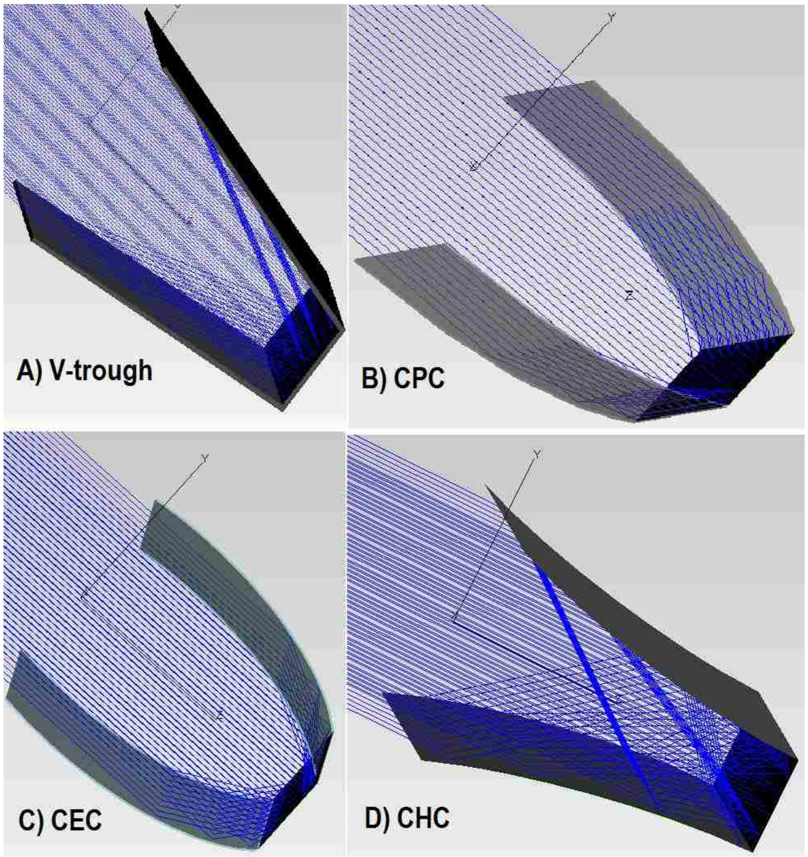

Figure 25 Hollow (no dielectric fill) nonimaging solar concentrators

The diurnal variations of the optical efficiency for the four simulated solid fill nonimaging concentrators and their hollow counterparts are shown on Figure 26 and Figure 27 respectively. Similarily, the diurnal variations of the optical concentration ratio for the four simulated solid fill nonimaging concentrators and their hollow counterparts are shown on Figure 28 and Figure 29 respectively. All the four figures underline a few important differences between solid and hollow nonimaging concentrators. The effective acceptance angle range for a solid fill geometry is much larger than a geometrically similar hollow design, thus enabling collection of more energy over a diurnal period as a stationary solar collector. However, the optical concentration ratio reaches the maximum possible value at normal incidence in hollow geometries rather than solid geometries due to the absence of Fresnel reflection losses. This merely suggests that hollow geometries would perform slightly better in a solar tracking application. Nonetheless, all the solid geometries trump their hollow counterparts as stationary concentrators enabling longer diurnal collection of solar energy. The ideal nonimaging collector – CPC has a well-defined acceptance angle range within which there is complete acceptance (barring Fresnel reflection losses in the solid fill CPC) of the incident étendue, and beyond which there is no acceptance at all. Other non-ideal nonimaging collectors (V-trough, CEC and CHC) are characterized by an additional transition acceptance region within which there is partial acceptance of the incident étendue. As expected, this transition region is much larger in the case of solid geometries compared to their hollow counterparts.

Table 2 Performance parameters – η_{opt}, CR_o, and diurnal energy collected for the 4-types of stationary nonimaging concentrators - solid (PMMA fill) and hollow (no fill).

Type of non-imaging concentrator geometry	**Average optical efficiency (η_{opt})**		**Average optical concentration ratio (CR_o)**		**Total diurnal energy collected (in kWh/m^2-day)**	
	Solid	Hollow	Solid	Hollow	Solid	Hollow
V-trough	0.6554	0.4640	1.475	1.044	9.16	6.49
CPC	0.6580	0.4633	1.481	1.042	9.20	6.48
CEC	0.6543	0.4634	1.472	1.043	9.15	6.48
CHC	0.6629	0.4640	1.492	1.044	9.27	6.49

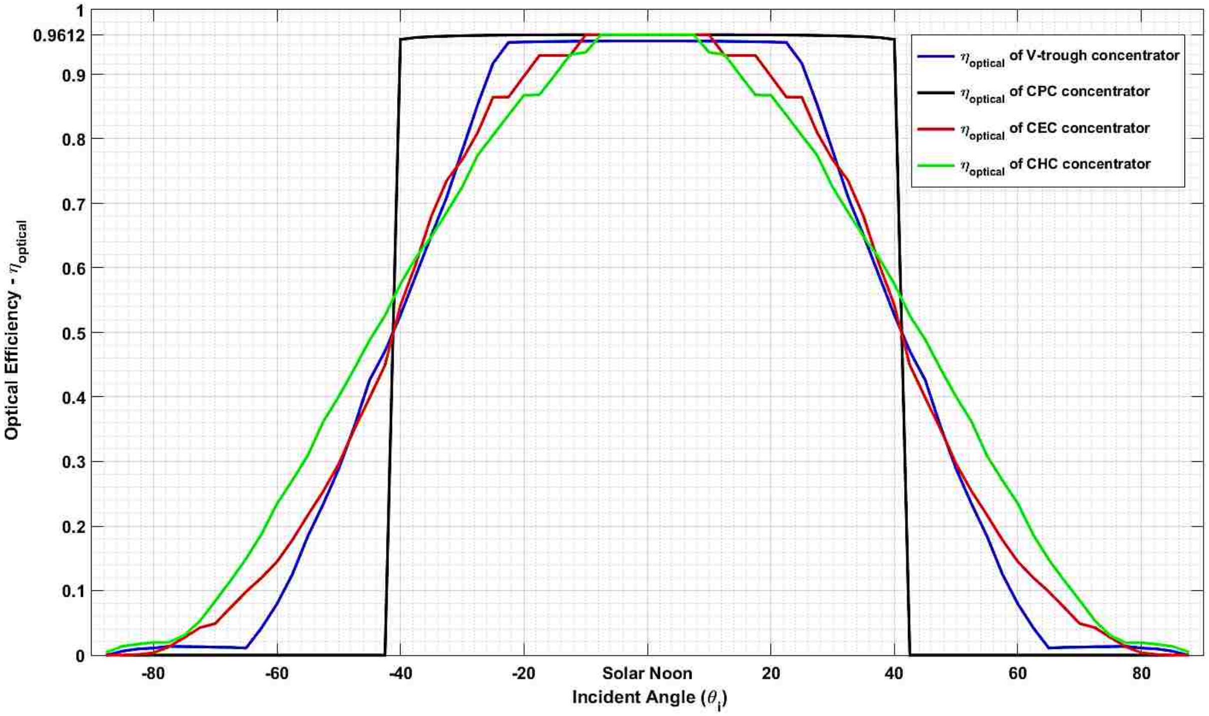

Figure 26 Variation of optical efficiencies with the angle of incidence in various nonimaging concentrators with RI=1.4805-1.5050 (PMMA solid fill)

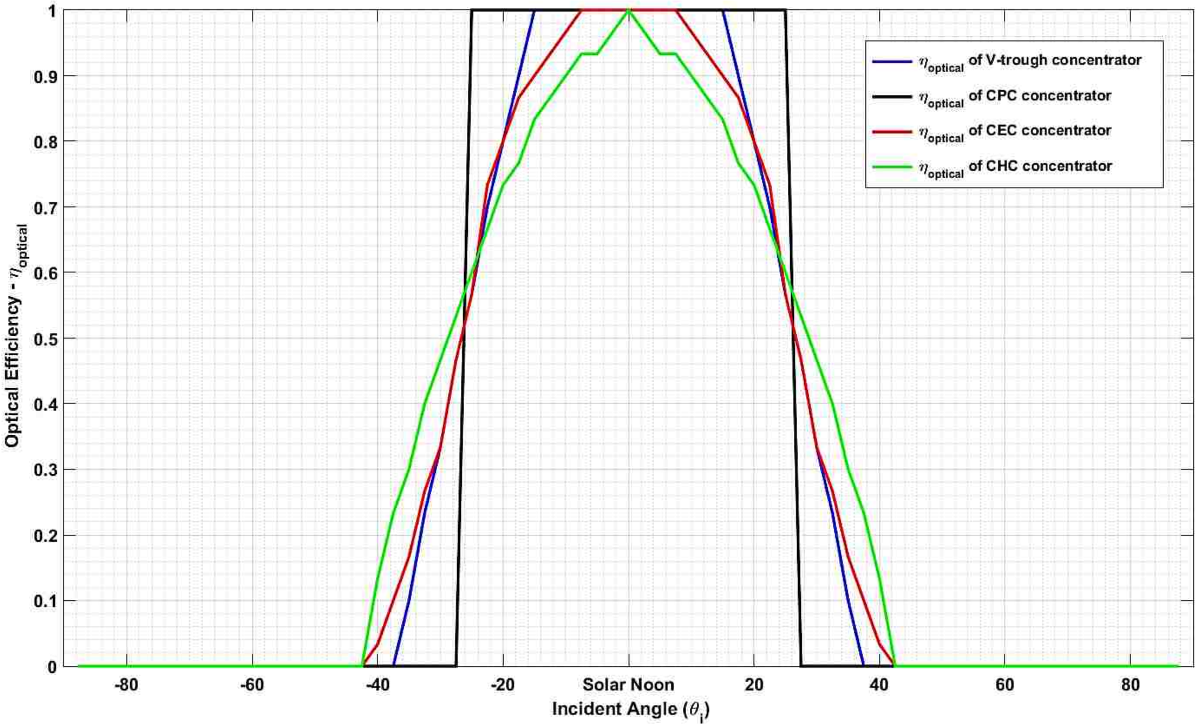

Figure 27 Variation of optical efficiencies with the angle of incidence in various nonimaging concentrators with no fill (hollow)

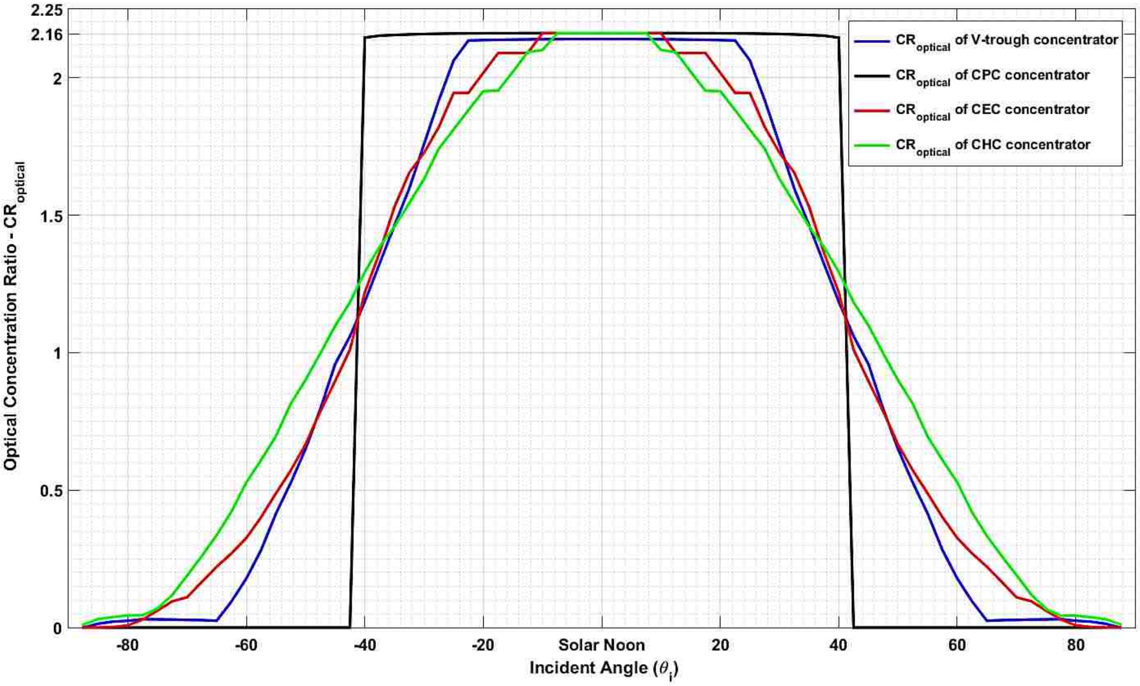

Figure 28 Variation of optical concentration ratios with the angle of incidence in various nonimaging concentrators with RI=1.4805-1.5050 (PMMA solid fill)

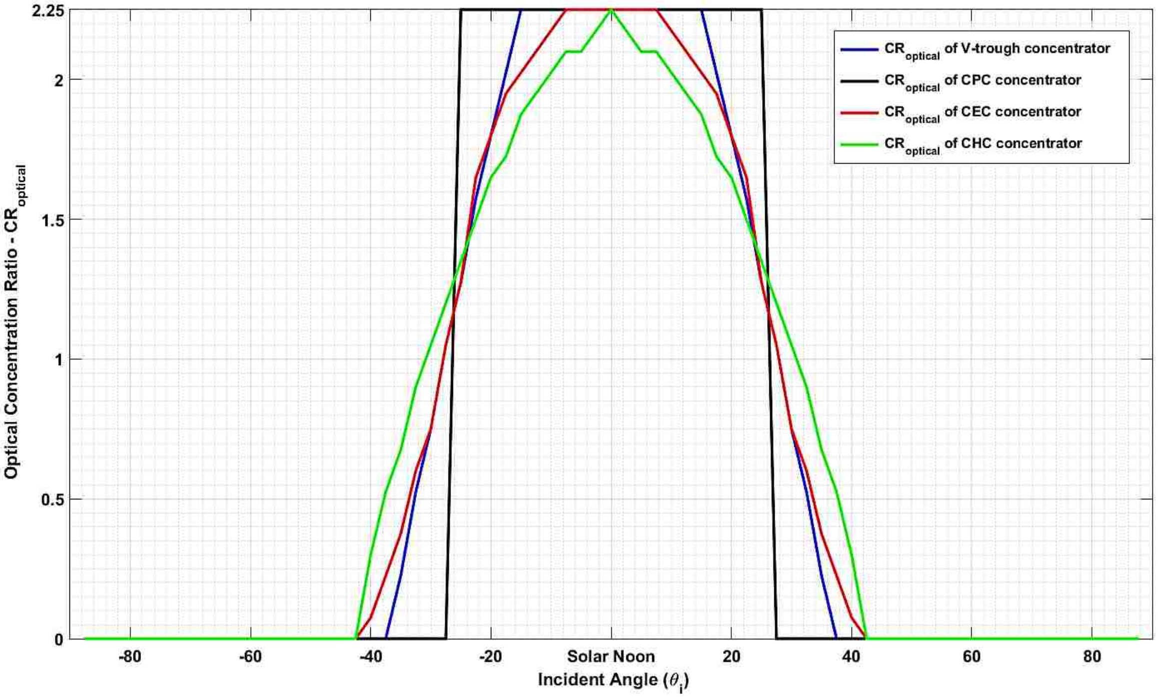

Figure 29 Variation of optical concentration ratios with the angle of incidence in various nonimaging concentrators with no fill (hollow)

4.4 Effect of Refractive Index on the Diurnal Energy Collection

As we have seen so far, solid nonimaging concentrators achieved better energy collection due to the virtue of the refractive index of the dielectric fill which is effectively increasing the acceptance angle. However, the refractive index of the dielectric material fill also induces the Fresnel reflection and TIR losses in the concentrator, thereby hampering energy collection. As an overall effect, the diurnal energy collection increases in all the four nonimaging concentrators with the increase in the refractive index of the dielectric material (used as a solid fill) until it reaches a threshold point of refractive index, after which the energy collection decreases. This threshold point of RI is different for all the four concentrator geometries. This overall effect of refractive index on the diurnal energy collection in all the four considered nonimaging geometries is illustrated on Figure 30. The reason for this reversal behavior is that the increment in energy collection due to higher acceptance angle can no more counteract the losses due to Fresnel reflection and total internal reflection beyond the threshold refractive index value. The absorber fluxes corresponding to various azimuth angular positions of the solar source, over the course of a day, is an output of the TracePro raytracing analysis. The total diurnal energy collection is evaluated through processing this data using (4).

$$Total\ diurnal\ energy\ \left(\frac{kWh}{m^2-day}\right)=\frac{\sum_{i=1}^{N_s}(\Phi_r/A_r)_{source_i}}{No.of\ Sources\ (N_s)\times 10^3}\times\frac{No.of\ hours}{day} \tag{4}$$

Figure 30 also emphasizes the fact that at lower refractive index values of the solid fill, the total diurnal energy collection is almost the same for the four considered nonimaging concentrator geometries. It should be noted that the geometric concentration ratio also has an effect on the threshold point of RI. For a given stationary nonimaging concentrator type, the greater the value of geometric CR, the larger is the threshold point value of RI.

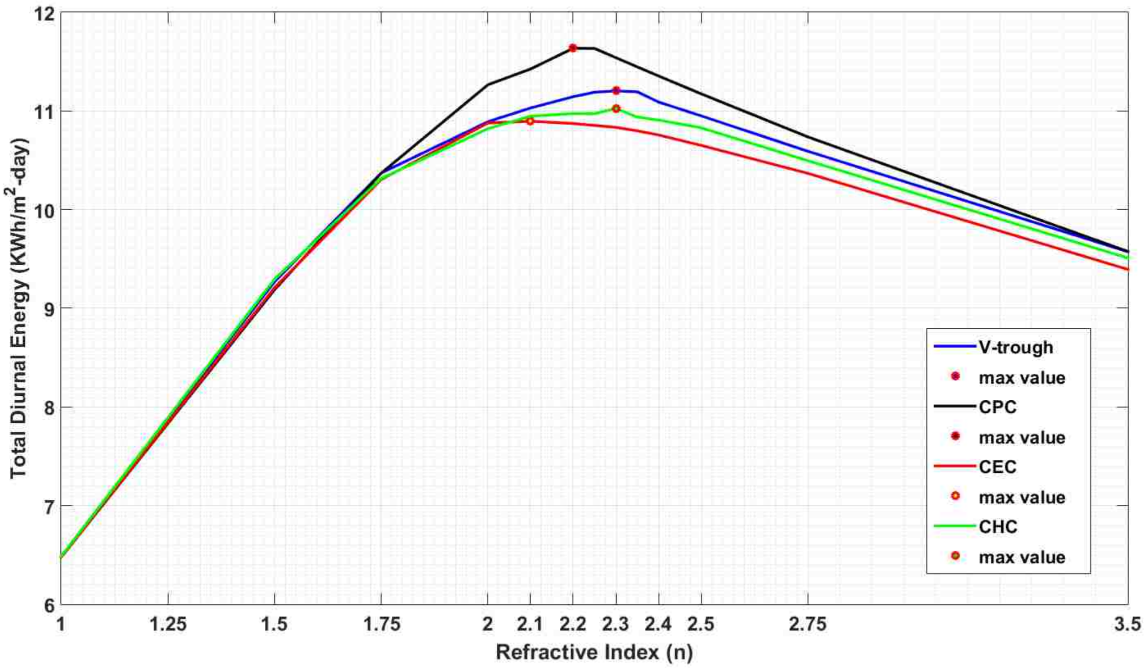

Figure 30 The total diurnal energy collected by solid dielectric nonimaging concentrators (CR=2.25) with various refractive indices

4.5 Results and Conclusions

The effect of Fresnel and total internal reflection losses on various stationary dielectric-filled (PMMA material, RI ~1.4805-1.5050) nonimaging type concentrators has been analyzed using TracePro raytracing software. The results show negligible difference among all the considered four different geometries namely – V-trough, CPC, CEC and CHC. However, a comparison with their hollow counterparts indicate that all the solid (PMMA fill) nonimaging concentrators collected about 1.41 to 1.43 times more energy. This analysis demonstrates that the dielectric nonimaging concentrators are better stationary diurnal energy collectors than their hollow counterparts. Furthermore, the effect of refractive index on the diurnal energy collection in all the four stationary nonimaging concentrators is analyzed. It is noted that for each of the concentrator geometries, there is a unique threshold refractive index value (between 2.1 and 2.3 for the considered geometric concentration ratio, CR=2.25) beyond which any increase in refractive index of the dielectric fill will only cause a decrease in the diurnal energy collection. This is due to the reason that increased amount of reflection losses (predominantly Fresnel reflection loss, and some TIR loss) are unable to counterbalance any energy gain due to effective increase in acceptance angle beyond the threshold refractive index value for the dielectric fill. The threshold refractive index is where the maximum diurnal energy collection happens in a stationary application for the given nonimaging collector geometries.

CHAPTER 5: IMPROVEMENTS IN STATIONARY CONCENTRATOR DESIGNS

In the previous chapter, we have proven that the dielectric filled solid nonimaging concentrators are better than hollow counterparts for stationary applications. However, the dielectric filled solid designs experience a substantial amount of Fresnel reflection losses when used as stationary concentrators. In order to mitigate these losses, two design improvements are proposed – (i) Graded refractive index films (GRIFs) on entry aperture, and (ii) stacked nonimaging concentrator designs. This chapter discusses these two improvements to the design of stationary dielectric nonimaging concentrators in detail. Both the design enhancements were modeled and simulated in TracePro to validate energy collection improvement.

In the previous chapter (refer to Figure 30), we have noticed that the dielectric solid CPC (CR=2.25) with higher refractive index material (n=2.2) yields even better collection compared to a PMMA fill (n=1.4805-1.5050). Although the peak concentration ratio is slightly below 1.9X, the energy collection happens throughout the day leading to higher energy collection – almost twice that of a flat plate. However, this energy collection could have been even higher if not for the Fresnel reflection at the entry aperture. In general, higher refractive index for the CPC fill material causes higher amount of Fresnel reflection and, thus, a certain decline in the overall energy collection at the absorber. In order to mitigate the Fresnel reflection losses, the aforementioned two design improvements are proposed. The following sections discusses these two approaches in detail.

5.1 Graded Refractive Index Films (GRIFs)

In 1880, Lord Rayleigh discovered that graded-refractive index layers have broadband antireflection properties by studying radiation passing through the Earth's atmosphere [35]. This idea is the basis for anti-reflective coatings (ARCs). A detailed review on the existing and technological advances in ARCs was presented by Raut et al. [36]. According to them, there are two typical ways of achieving anti-reflection. Firstly, by changing the physical attributes of the entry aperture surface using nano-grade porous or patterned coatings. Porous graded silicon (P-Si) is a popular anti-reflective coating (ARC) material of this type. Also, nanostructure patterns or sub-wavelength structures such as silicon nanotips developed by Huang et al. [37] through biomimicry of the outer surface of a moth's corneal lens falls under this category as well. Secondly, anti-reflection can also be imparted by using a multi-layered graded refractive index (GRIN) structure as a superstrate at the entry aperture. Materials such as magnesium fluoride (MgF_2), cerium oxide (CeO_2), zinc sulphide (ZnS) and silicon mono oxide (SiO) are commonly used in tandem as single or double-layered ARCs. Titanium oxide (TiO_2) has been widely used on high refractive index substrates such as silicon. Other infrequently used ARCs include organic films of long chain fatty acids, surface porous polystyrene/poly(vinylpyrrolidone) (PS/PVP) polymer films, gallium and indium based ARCs etc. ARCs are typically designed to operate under certain radiation wavelength ranges at certain angles of incidence, and polarization. Efforts have been made to create omnidirectional ARCs with a wide spectral range. Researchers [38] were able to numerically investigate various designs of such ARCs. It was shown that inhomogeneous-layer ARCs with 4-7 layers of different refractive index materials can shrink the Fresnel reflective losses to below 10% for a wide range of angular ([-85°, 85°]) and spectral incidence (5.0-8.0 µm).

The refractive indices (at midpoints of the transparency ranges) of some commonly used optical materials are listed on Table 3. The materials tabulated are non-absorbing in most regions of the UV, the visible and the IR spectra. These materials can be selected suitably to design a graded refractive index film (GRIF). Two such films – one comprising 3-layers, and another comprising 1-layer – were designed in TracePro environment. These GRIFs act as antireflective coatings for high RI dielectric stationary nonimaging concentrators thereby enhancing their diurnal energy collection. The results of the raytracing analysis are discussed in section 5.3.1.

Also, Figure 31 was constructed in the TracePro environment to measure the effect of graded refractive index film on an absorber surface. About 709000 rays were incident on the top surface of the film at various incident angle ranging from [-87.5° to 87.5°], and the effect on the absorber surface is examined as shown on Figure 32. About 7.2% of the incident flux on the top surface will be reflected at various interfaces (from the top surface for most angles). Comparatively, if the refractive index film of the same combined thickness of 5 μm and a constant refractive index of n=1.9 (maximum refractive index) was used, a higher loss of the incident flux of about 12.5% is noticed. Therefore**,** in concentrator applications where high refractive index optics interact with air, the Fresnel reflection at the entry aperture surface can be minimized by the application of these types of films.

Table 3 Refractive indices of some commonly used optical multilayer coating material.

Multi-layer optical coating material	**Refractive index (n)**	**Multi-layer optical coating material**	**Refractive index (n)**
cryolite	1.35	HfO_2	1.98
LiF	1.37	Ta_2O_5	2.1
MgF_2	1.39	ZrO_2	2.1
SiO_2	1.48	CeO_2	2.2
ThF_4	1.52	Nb_2O_5	2.2
Al_2O_3	1.6	ZnS	2.3
CeF_3	1.62	TiO_2	2.45
MgO	1.72	ZnSe	2.55
PbF_2	1.73	Si	3.5
Y_2O_3	1.82	Ge	4.2
Sc_2O_3	1.86	Te	4.8
SiO	1.95	PbTe	5.5

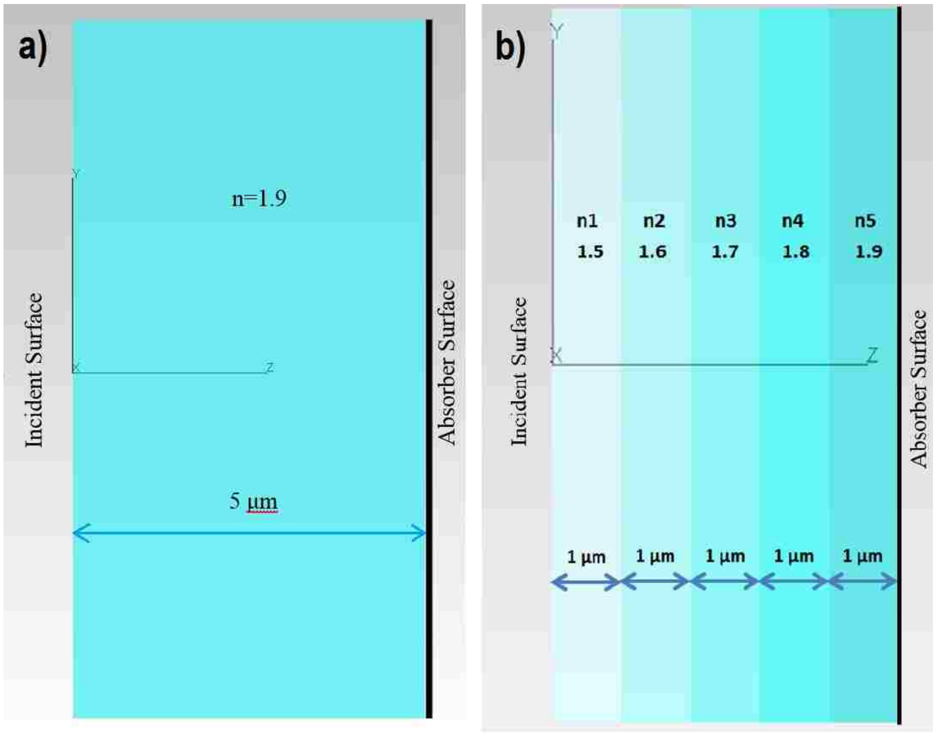

Figure 31 (a) A 5-micron thick constant refractive index film and (b) variable refractive index film

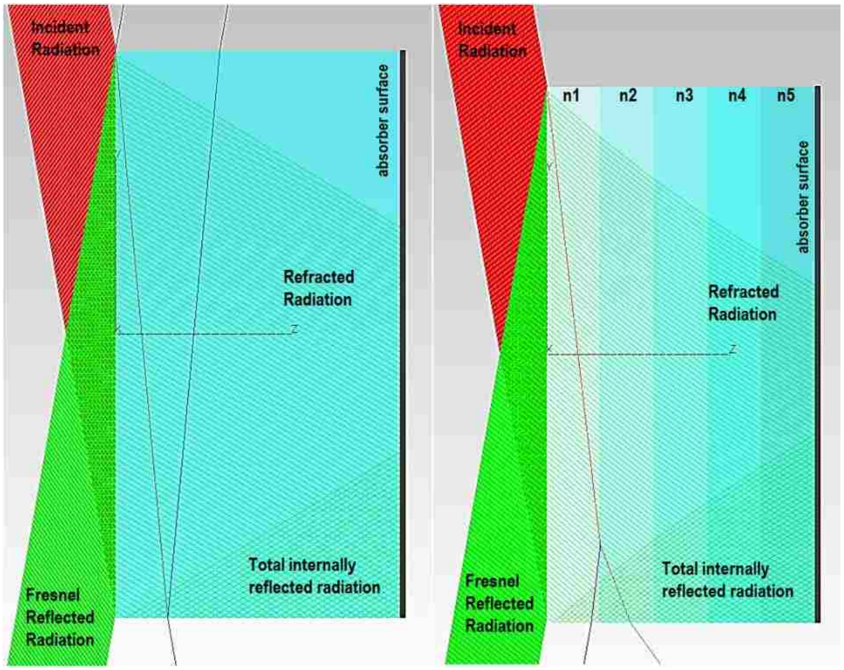

Figure 32 Comparing the Fresnel reflection at angle of incidence of 80° for both (a) constant and (b) variable refractive index films

5.2 Stacked Nonimaging Concentrator Design

There are two types of stacked nonimaging concentrator designs discussed in this section. The first one is a stacked CPC design and the second one being the stacked V-trough design. It should be noted that the V-trough design is a simplification of the parabolic profile to a linear profile in the design.

5.2.1 Stacked CPC Design

Assume that there are ‘N’ number of divisions in a stacked CPC design as shown in Figure 33. Each of the partition is a CPC by itself, and there are ‘N’ number of them in this design with θ_{a1}, θ_{a2}, θ_{a3}…. θ_{aN} being the respective acceptance half angles, and n_1, n_2, n_3…. n_N being the respective refractive indices of the individual CPCs in the stack. The width of the top layer (entry aperture) is d_1 and the bottom layer (exit aperture or absorber) is d_{N+1} while all the intermediate interface dimensions are labelled d_k where k=2,3,4…N. Now, it will be demonstrated (as a special case) in the following discussion that, mathematically speaking, stacking of hollow CPCs is not of much benefit for energy collection.

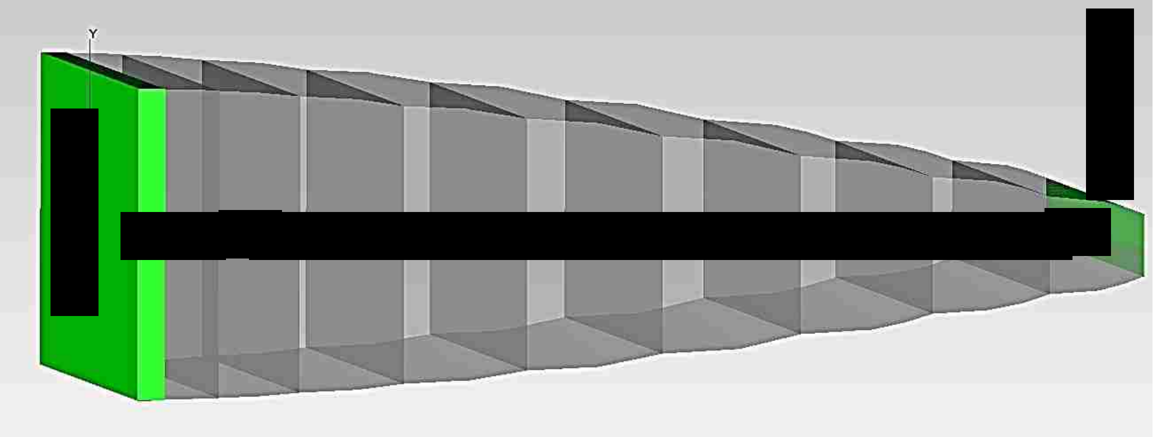

[redacted]
[redacted]
[redacted]

Figure 33 Stacked CPC design

From Winston’s research [39] on dielectric CPCs, we understand that the geometric CR (= entry aperture area/exit aperture area) for any individual CPC in the stack can be written as:

$$\frac{d_k}{d_{k+1}} = \frac{n_k}{\sin(\theta_{ak})}$$

Where $k = 1, 2, 3 \ldots\ldots\ldots N$. If we multiply individual geometric CR values,

$$\frac{d_1}{d_2} \times \frac{d_2}{d_3} \times \frac{d_3}{d_4} \cdots \times \frac{d_N}{d_{N+1}} = \frac{n_1}{\sin(\theta_{a1})} \times \frac{n_2}{\sin(\theta_{a2})} \times \frac{n_3}{\sin(\theta_{a3})} \ldots\ldots \times \frac{n_N}{\sin(\theta_{aN})}$$

$$\sin(\theta_{a1}) \times \sin(\theta_{a2}) \times \ldots\ldots \times \sin(\theta_{aN}) = \frac{d_{N+1}\,(n_1 n_2 n_3 \cdots n_N)}{d_1}$$

$$= \left(\frac{n_{eff}\, d_{N+1}}{d_1}\right)\left(\frac{n_1 n_2 n_3 \cdots n_N}{n_{eff}}\right)$$

$$= \sin\left(\theta_{eff}\right) \left(\frac{n_1 n_2 n_3 \cdots n_N}{n_{eff}}\right)$$

$$\therefore \frac{\sin\left(\theta_{eff}\right)}{n_{eff}} = \frac{\sin(\theta_{a1})}{n_1} \times \frac{\sin(\theta_{a2})}{n_2} \times \frac{\sin(\theta_{a3})}{n_3} \cdots \times \frac{\sin(\theta_{aN})}{n_N}$$

$$= \prod_{k=1}^{N} \frac{\sin(\theta_{ak})}{n_k} \ldots \boldsymbol{Eq}\ (\mathbf{1})$$

This can also be written as:

$$CR_{eff} = \prod_{k=1}^{N} CR_k$$

Special Case:

If all n$_k$ and n$_{eff}$ are 1, which pertains to a hollow stacked CPC as shown in Figure 34, then:

$$\sin\left(\theta_{eff}\right) = \prod_{k=1}^{N} \sin(\theta_{ak})$$

Now noting that $0 < \sin(\theta_{ak}) < 1$, $\prod_{k=1}^{N} \sin(\theta_{ak})$ will always be less than individual $\sin(\theta_{ak})$ and, hence, the effective acceptance angle, θ_{eff} will be lower than any individual θ_{ak}. In conclusion, stacking of hollow CPCs is counterproductive as it will reduce the effective acceptance angle and is especially not appropriate for stationary applications. Also, the exit rays from a preceding top CPC to a succeeding bottom

CPC are at a much widely spread étendue compared to the original étendue from the radiation source. So unless, there is some refraction phenomenon involved at the interface of two adjacent CPCs, the étendue remains wide spread. Therefore, stacked CPC design is productive only when it is a solid design with a transparent dielectric fill material.

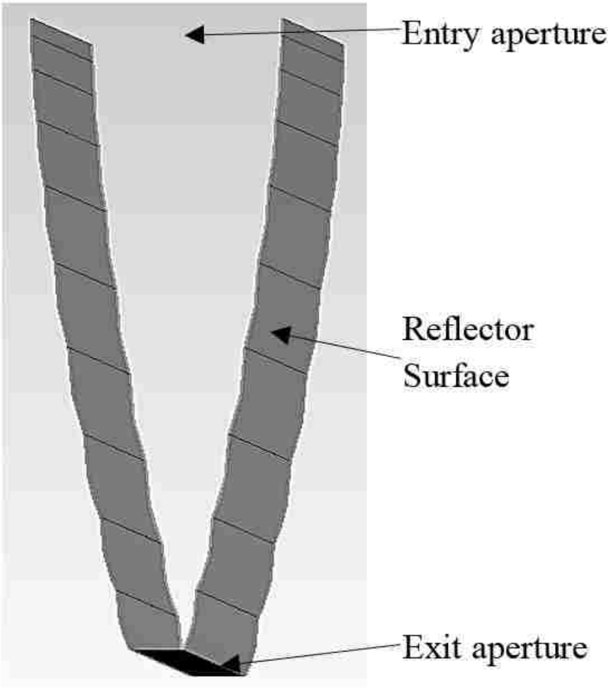

Figure 34 Hollow Stacked CPC design

5.2.2 Stacked V-trough Design

The stacked V-trough design is a simplification of the stacked CPC design. The parabolic profile between any two adjacent interfaces is simplified to a linear profile. This will help in easier manufacturing of a prototype. The stacked V-trough design is shown on Figure 35. It should be noted that this design is not the stacking of individual V-troughs but an approximation of the CPC’s parabolic profile to a linear profile. It is a piece-wise linear assumption of the polynomial profile that connects the end points of the entry and exit apertures while passing through all the intermediate aperture end points.

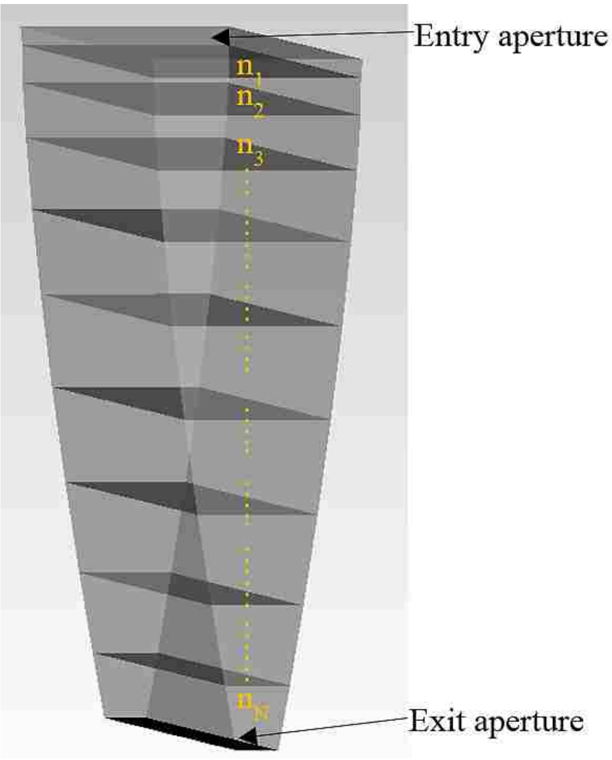

Figure 35 Stacked V-trough design

5.2.3 Degrees of Freedom

Both the stacked dielectric nonimaging concentrator designs have $\{2N+1\}$ degrees of freedom that can be altered in the design. Those are:

i) Entry aperture dimension (d_1) - 1

ii) Exit aperture dimension (d_{N+1}) - 1

iii) Refractive indices of individual CPCs (n_1, n_2, $n_3 \ldots n_N$) - N

iv) Intermediate dimensions (d_2, $d_3, \ldots . d_N$) - (N-1)

So the design optimization problem has too many variants to optimize. However, a few of these variants can be assumed invariable and, consequently the other degrees of freedom will yield in a partially optimized design. For instance, the dimensions and the number of partitions can be assumed constant while the refractive indices can be varied.

5.3 Results from TracePro Raytracing Simulations Analysis

TracePro raytracing program was used to model both the stacked designs as well as graded refractive index films on high RI nonimaging concentrators. The results obtained show improvement in energy collection in both cases.

5.3.1 Graded Refractive Index Films Simulation Analysis

All the stationary dielectric-filled nonimaging concentrators modeled in the previous chapter have not been subject to any measures to reduce the Fresnel reflection losses at the entry aperture. However, adding a graded refractive index film (GRIF) as a superstrate on the entry aperture is a step in that direction. The four nonimaging concentrators were modeled to be simulated under the influence of a single-layer GRIF, and a triple-layer GRIF. The entry aperture is coated with a single-layer of MgF_2 (thickness=0.0912 µm) in the first simulation, and with respective layers of Al_2O_3 (thickness=0.0769 µm, closest to substrate), ZrO_2 (thickness=0.125 µm) and MgF_2 (thickness=0.0912 µm, closest to the incident medium) to form a triple-layer GRIF in the second simulation. Application of GRIFs show the following improvements in the dielectric solid filled nonimaging concentrators as enumerated on Table 4 and Table 5.

Table 4 Improvement in high RI nonimaging concentrators with application of 1-layer GRIF

Type of non-imaging concentrator geometry	**Average optical efficiency (η_{opt})**		**Average optical concentration ratio (CR_o)**		**Total diurnal energy collected (in kWh/m^2-day)**	
	Solid	With GRIF 1-layer	Solid	With GRIF 1-layer	Solid	With GRIF 1-layer
V-trough	0.8013 (RI=2.3)	0.8888 (RI=2.35)	1.803	2.000	11.20	12.43
CPC	0.8322 (RI=2.2)	0.9194 (RI=2.25)	1.872	2.069	11.63	12.86
CEC	0.7793 (RI=2.1)	0.8539 (RI=2.35)	1.753	1.921	10.90	11.94
CHC	0.7886 (RI=2.3)	0.8706 (RI=2.3)	1.774	1.959	11.03	12.17

Table 5 Improvement in high RI nonimaging concentrators with application of 3-layer GRIF

Type of non-imaging concentrator geometry	**Average optical efficiency (η_{opt})**		**Average optical concentration ratio (CR_o)**		**Total diurnal energy collected (in kWh/m^2-day)**	
	Solid	With GRIF 3-layer	Solid	With GRIF 3-layer	Solid	With GRIF 3-layer
V-trough	0.8013 (RI=2.3)	0.8888 (RI=2.35)	1.803	2.000	11.20	12.43
CPC	0.8322 (RI=2.2)	0.9194 (RI=2.25)	1.872	2.069	11.63	12.86
CEC	0.7793 (RI=2.1)	0.8539 (RI=2.35)	1.753	1.921	10.90	11.94
CHC	0.7886 (RI=2.3)	0.8706 (RI=2.3)	1.774	1.959	11.03	12.17

The results of both the simulations are further summarized as Figure 36 and Figure 37. It can be noticed from these figures that the application of GRIFs enhanced the total diurnal energy collection in both the cases. Furthermore, the percentage increases in the total diurnal energy collection with application of single-layered and triple-layered GRIFs (in all the four nonimaging concentrators) compared to the no GRIF application case are shown in Figure 38 and Figure 39 respectively. As expected, the GRIFs improved the energy collection performance better for higher RI solid fill cases mitigating the higher Fresnel reflection losses that are encountered. It is also interesting to note that the chosen triple-layer GRIF would fail to perform better than the no GRIF case for lower RI (below 1.62) solid fill cases. Another interesting observation can be made comparing the trends of Figure 30, Figure 36 and Figure 37. All of them seem to peak at some refractive index value between 2 and 2.5. Beyond these threshold RI values, there seems to be no increase in energy collection despite the increase in RI value. There is a minor right shift in the threshold RI values when GRIFs are applied compared against a no GRIF application case. The threshold RI values are the same in both single-layer and triple-layer GRIF application cases.

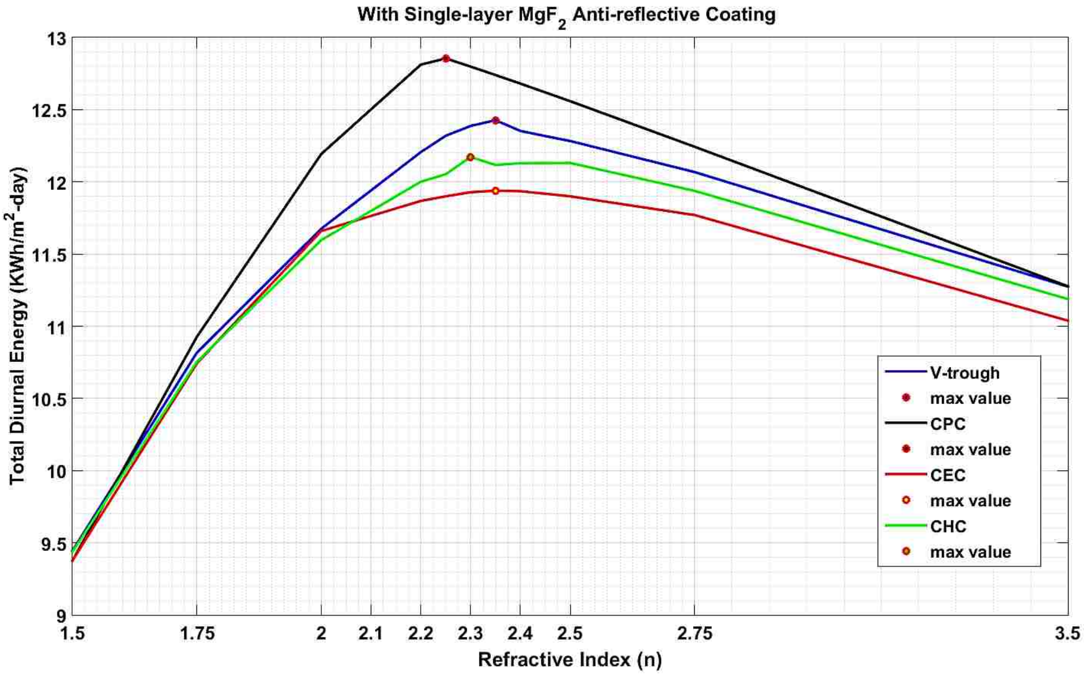

Figure 36 The total diurnal energy collected by solid dielectric nonimaging concentrators (CR=2.25) with various refractive indices where entry aperture is coated with single-layer MgF_2 GRIF

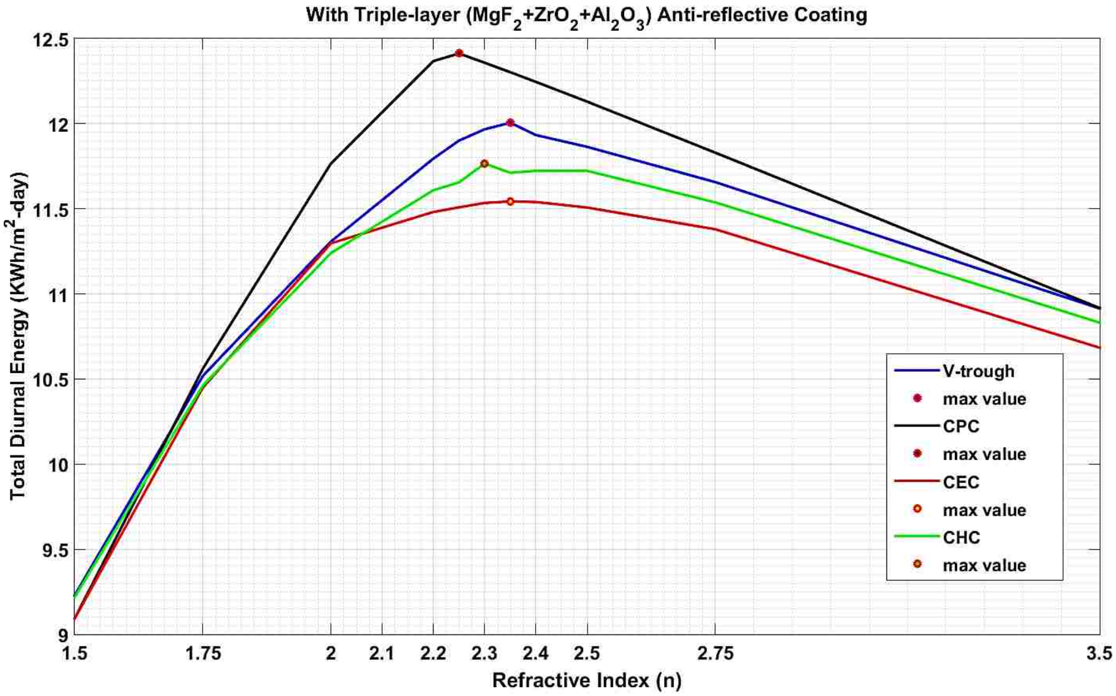

Figure 37 The total diurnal energy collected by solid dielectric nonimaging concentrators (CR=2.25) with various refractive indices where entry aperture is coated with multi-layer (Al_2O_3+ZrO_2+MgF_2) GRIF

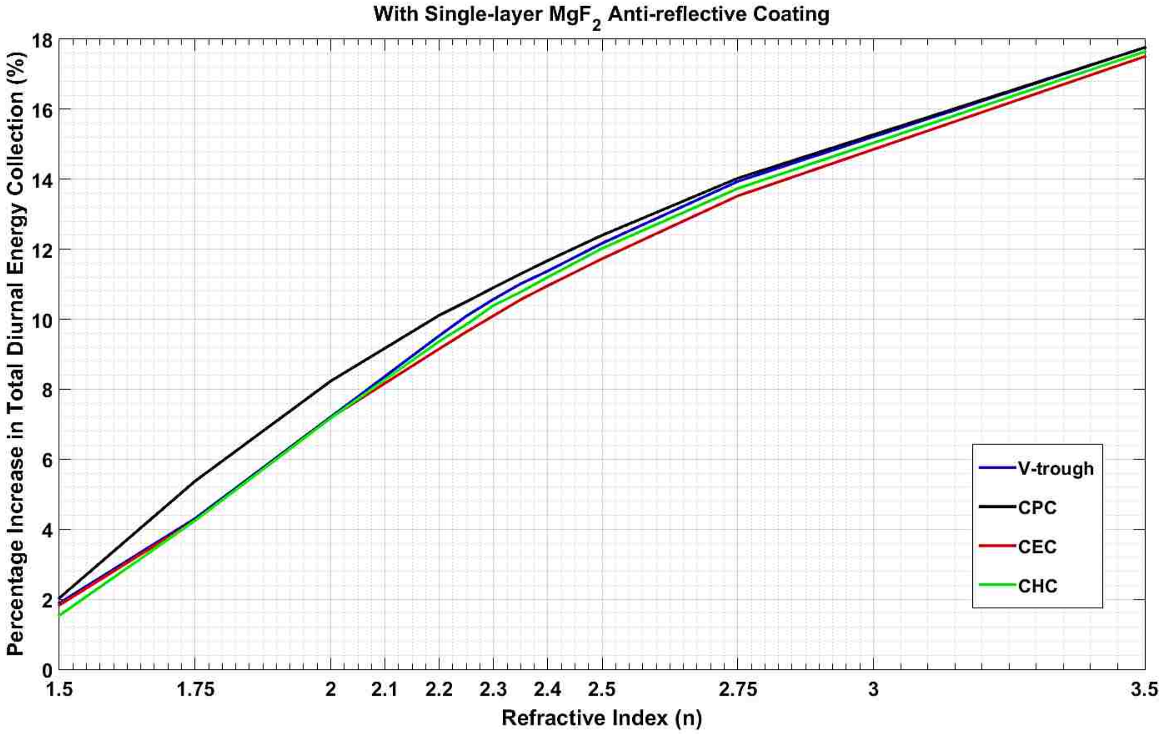

Figure 38 Percentage increase in the total diurnal energy collection due to the application of single-layer GRIF

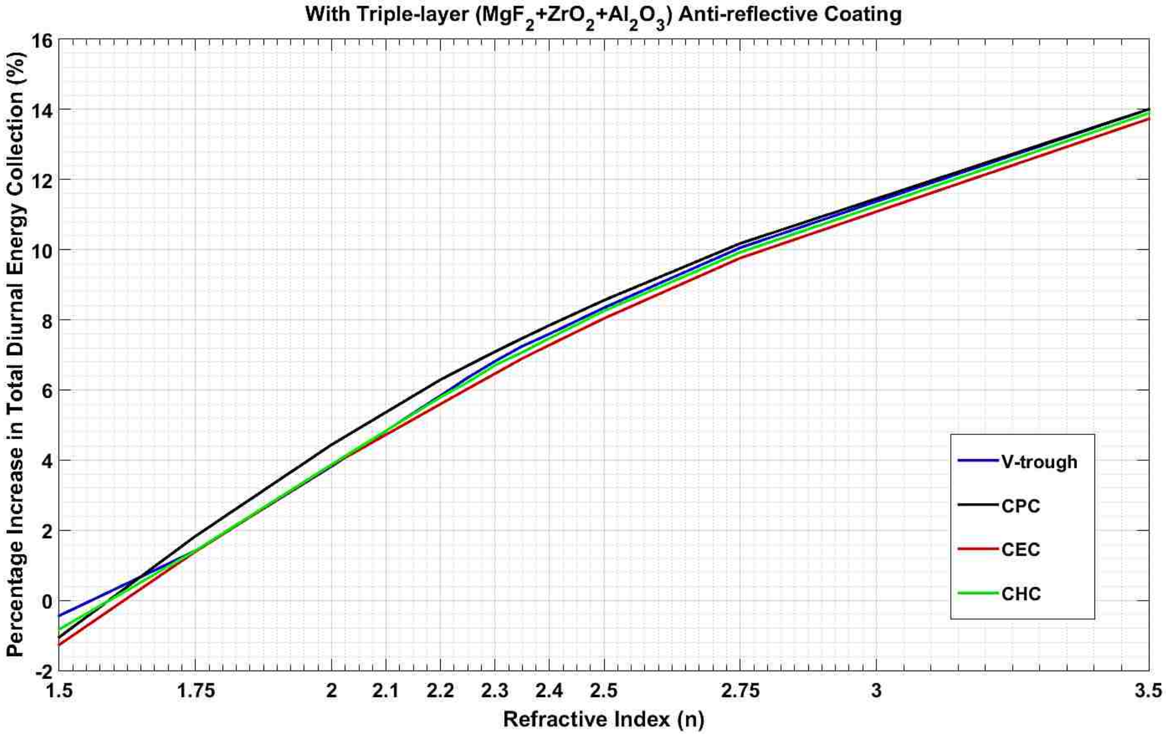

Figure 39 Percentage increase in the total diurnal energy collection due to the application of triple-layer GRIF

Although GRIFs improve the energy collection performance of a nonimaging collector by reducing Fresnel reflection at the entry aperture, the problem with most GRIFs is that they are designed to cater a certain range of wavelengths within certain range of angles of incidence, and with affinity to a certain type of polarization. This is not desirable when designing a stationary concentrator for the solar spectrum encompassing a wide range of wavelengths and angles of incidence. Therefore, in the given state-of-the-art, GRIFs can only be a partial solution to the problem of Fresnel reflection loss when applied to stationary nonimaging solar concentrators. In order to improve the diurnal energy collection, application of anti-reflective coatings over the entry aperture was investigated. GRIFs could partially alleviate the problem of Fresnel reflection loss and thus, improve the energy collection by 2 to 18% (single-layer GRIF) and -2 to 14% (Triple-layer GRIF) compared to the no GRIF case over the investigated range of refractive indices.

5.3.2 Stacked Nonimaging Concentrator Simulation Analysis

The stacked nonimaging concentrator designs of both CPC and V-trough are simulated in TracePro environment and the results are further analyzed using MATLAB programming. The optical efficiency, the optical concentration ratio and the diurnal energy collection in both the stacked nonimaging concentrator designs are evaluated.

With the number of partitions, N=10; entry aperture dimension, d_1=10 mm; exit aperture dimension, d_{11}=2 mm; and the intermediate dimensions were modeled using a 5° variation in the acceptance angle between two adjacent CPCs. The top-most CPC has an acceptance angle of 85° and the bottom-most CPC has an acceptance angle of 40°. As discussed before, the exit aperture of the k^{th} CPC becomes the entry aperture of the $k+1^{th}$ CPC where k=1,2,3,…9. In case of the stacked V-trough design, the parabolic profiles in the existing stacked CPC design are replaced by linear profiles. The refractive index starts at an initial value of 1.3 for the top CPC, and varies in steps of 0.1, 0.2 and 0.3 in the three considered cases respectively. All these simulations are carried out and the results are shown on Table 6. The results suggest that the larger the value of ΔRI, the higher is the value of the optical efficiency and the diurnal energy collection while keeping the dimensional parameters constant.

Table 6 Performance parameters of stacked nonimaging concentrator designs

Type of non-imaging concentrator geometry	**Average optical efficiency (η_{opt})**		
	With ΔRI=0.1 N=10	With ΔRI=0.2 N=10	With ΔRI=0.3 N=10
Stacked V-trough	0.4776	0.6136	0.7761
Stacked CPC	0.4554	0.5772	0.6989
Comparative solid CPC with highest RI	0.3981	0.4802	0.5313
Type of non-imaging concentrator geometry	**Average optical concentration ratio (CR_o)**		
	With ΔRI=0.1 N=10	With ΔRI=0.2 N=10	With ΔRI=0.3 N=10
Stacked V-trough	2.388	3.068	3.881
Stacked CPC	2.277	2.886	3.494
Comparative solid CPC with highest RI	1.990	2.401	2.657
Type of non-imaging concentrator geometry	**Total diurnal energy collected (in kWh/m^2-day)**		
	With ΔRI=0.1 N=10	With ΔRI=0.2 N=10	With ΔRI=0.3 N=10
Stacked V-trough	14.84	19.07	24.12
Stacked CPC	14.15	17.93	21.72
Comparative solid CPC with highest RI	12.37	14.92	16.51

CHAPTER 6: SUMMARY OF RESULTS AND CONCLUSIONS

The goal of this dissertation is to design stationary nonimaging concentrators that can achieve higher energy collection. This goal has been achieved through the proposed two design enhancements – stacked nonimaging concentrator designs and application of GRIFs on the entry aperture of the high RI nonimaging concentrators.

The methodology followed in achieving the solutions is described briefly. From the literature review, it was realized that the nonimaging solid dielectric fill concentrators are suitable for stationary solar concentration applications. Four commonly used geometries were chosen for further investigation. The increased acceptance angle due to the increase in refractive index of the dielectric fill material was studied further. Increase in acceptance angle means an increase in the diurnal energy collection. However, it was soon found that the energy collection increases with increasing RI only until the dominance of Fresnel reflection triumphs over. So the intermediate goal became the mitigation of the Fresnel reflection losses in order to achieve higher diurnal energy collection. The two proposed design approaches successfully achieved this higher energy collection and, thus, are suitable as stationary concentrators. The future research on these designs should try and solve the material constraints imposed.

The typical peak concentration ratios achieved through stationary dielectric concentration systems are between 3 to 10X. The concentration ratios higher than 10X can be achieved at the expense of duration of diurnal energy collection which is not generally desirable for a stationary concentration system. Although higher refractive index value of the dielectric fill material partially addresses this problem by increasing the duration of diurnal energy collection, it is still a highly material problem to find suitable high refractive index material. With the currently available advancements in material technology, concentration ratios between 3 to 10X can be safely achieved using stationary systems with longer diurnal energy collection times.

CHAPTER 7: APPLICATIONS AND FUTURE WORK

Coincidentally, CPC design is a biomimicry of the ommatidium in the compound eye of a horse-shoe crab that evolved millions of years ago. Since the invention and application of the earliest nonimaging concentrator - CPC to collect solar energy, various nonimaging collectors have seen diverse applications as solar energy collectors. Solar-pumped lasers are setup using nonimaging Fresnel lenses [40]. Other applications involve concentrated photovoltaics, solar thermophotovoltaic systems etc.

7.1 Fields of Application

Demonstration of building integrated photovoltaics with a stationary arrangement of nonimaging concentrators was conducted using two different concentrator designs – a linear convex Fresnel lens (10X concentration) and a combination of linear convex Fresnel lens (5X concentration) with CPC (2X concentration) [28].

Buildings in non-seismic, snow accumulation regions (typically higher latitude regions) are most suitable for installing a mid-temperature range (80 to 250 °C) stationary nonimaging solar collector [41]. Four different nonimaging collector configurations - CPC, sea shell with upper reflector, sea shell with adjustable reflector and vertical asymmetric CPC - coupled with evacuated tubes were considered as a part of a case study for building integration. The suitable building types, structural and reflector details were discussed.

Solar photocatalytic detoxification of water is the removal of hazardous and non-biodegradable wastes using the near-ultraviolet band of the solar spectrum (wavelength under 390 nm). The UV radiation photoexcites a semiconductor catalyst (typically TiO_2) to promote oxidative and reductive reactions. Under the SOLARDETOX project, a detoxification plant was built that incorporated two rows of 21 modules of cusp type CPC collectors (oriented in E-W direction) with a total aperture area of 100 m^2 and a loop capacity of 800 liters/cycle [42]. Prospective application of the nonimaging optics in laser fiber optic surgical procedures was discussed [43]. The increase in irradiance with maximum collection efficiency and uniform distribution over a wider angular range are the motivating factors when compared to imaging optics or tapered V-cone type devices.

A lithium bromide-water (LiBr-H_2O) based solar absorption cooling system was coupled with CPC solar collectors with evacuated tube receivers and tested in Jinan City, China (36.65° N, 117.12° E) [44]. The CPC solar collectors (105 m^2) that were oriented in N-S direction at a tilt angle of 20° achieved an average cooling capacity of 9.2 kW at a COP of 0.19. These systems provided chilled water at 15 °C from 11 AM to 3:30 PM. The thermal efficiency of the CPC collectors was comparatively higher than a traditional collector at higher operating fluid (water) temperatures.

7.2 Passive solar tracking coupled nonimaging concentration systems

Although the focus of this dissertation is on stationary nonimaging concentration systems, it is only relevant to include some discussion on advancements in passive solar tracking systems as they are a particularly attractive option, owing to their simplistic, low-cost design, in ramping up the collector concentrations. As opposed to the active solar tracking mechanism which uses certain portion of the auxiliary power (electrical power) to drive it's tracking mechanism, the passive solar tracking mechanism is driven by changing physical attributes due to the diurnal motion of the sun.

Passive solar tracking systems are based on differential thermal expansion of materials such as refrigerants, bimetallic strips or shape memory alloys. The mechanism usually comprises two actuators working against each other. When there is unequal illumination of the actuators, there are unbalanced forces generated causing the reorientation of the apparatus in such a direction where equal illumination of actuators, and the balance of the forces are restored. They are inexpensive and less complex compared to active trackers but are also less efficient. Also, since they are thermally activated mechanisms, ambient temperature variations can affect their functionality. Clifford et al. [45] designed a passive solar tracking system which increased the energy output of the solar panels by 23% compared to a fixed system. However, incorporating a night return mechanism and a dual axis tracking mechanism are the future challenges for this design. The drying time of coffee beans is reduced by 2-3 days using a manually adjustable (with 15° increment) single-axis tracking system [46]. Shape memory alloy actuators were used to design another passive solar tracking system. A tracking accuracy of ±5° was achieved using these systems. The inherent disadavantage of less precise tracking of passive tracking systems can be over come by coupling with nonimaging concentrators. The most popular passive solar tracking mechanisms are categorized as shown in Figure 40 [45][46][47][48].

The acceptance angle of a nonimaging concentrator can be the maximum permissible tracking error for a passive solar tracking system oriented in N-S direction. Figure 41 shows the maximum concentration ratio attainable as a function of the maximum permissible tracking error in case of a CPC concentrator and passive tracking system coupling. Hence, given the low-cost of the passive tracking systems, coupling them with nonimaging concentrators is a viable option to achieve low to moderate concentrations.

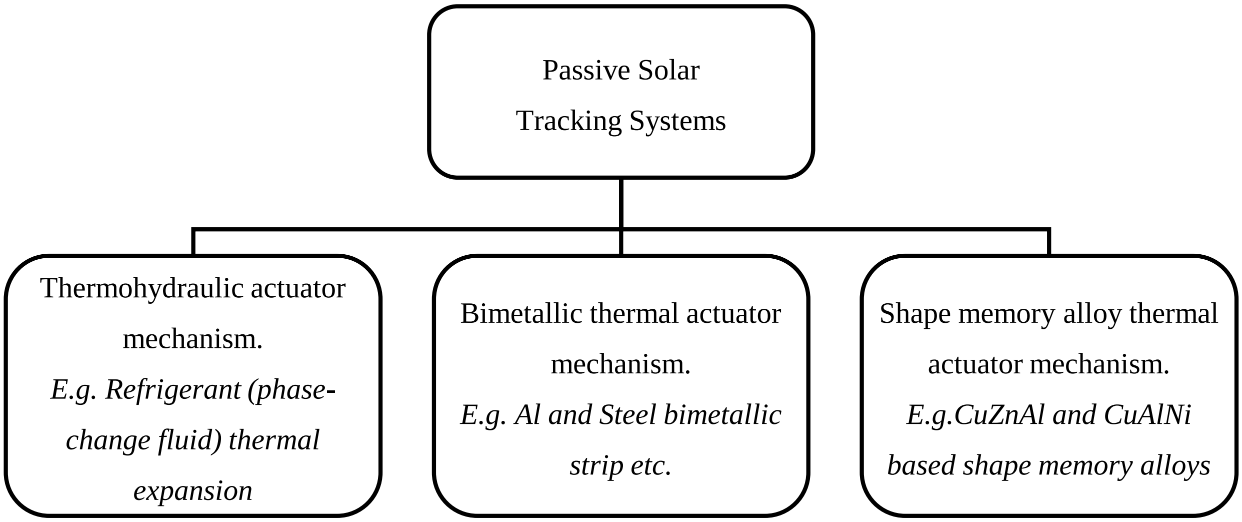

Figure 40 Classification of passive tracking systems

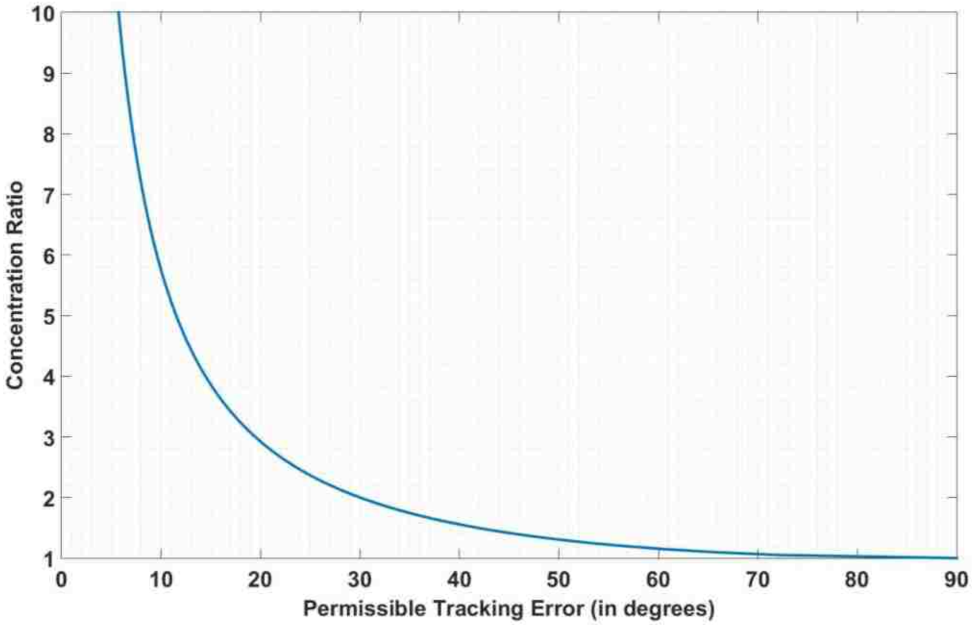

Figure 41 Permissible single-axis tracking error vs. the achievable max. concentration ratio in a scenario of passive solar tracking system coupled with a hollow CPC concentrator

7.3 Materials Selection

The improvement of energy collection in nonimaging optics is as much a material selection problem as it is a solid modeling problem. Since the solar spectrum has a range of 250-8000 nm, the material with minimum optical losses in this region should be considered for application as concentrator material. The future work on this topic should explore transmission, absorption, and scattering losses in real world material. Although, the transmission, absorption and scattering losses have been considered for a few commonly used dielectric materials by using the respective attenuation coefficients and the bidirectional scatter distribution functions (BSDF) in the simulation, future work should explore more detailed analysis of optical material to quantify the effects of attenuation and scattering in nonimaging stationary concentrators.

The optical properties of some of the commonly used material such as poly methyl methacrylate (PMMA), polystyrene (PS), polycarbonate (PC), styrene acrylonitrile (SA) and borosilicate crown glass (BK7) are enumerated in Table 7 [49]. Good et al. [50] discussed the spectral reflectance, transmittance and angular scattering of some commonly used reflective materials in solar concentrators. They also discussed the spectral transmittance of two transparent 100 micron thin films namely, ethylene-tetrafluoroethylene (ETFE) and fluorinated ethylene propylene (FEP). The solar-weighted (spectrally) values of the transmittance in semi-transparent materials and specular reflectance of reflective materials at various angles of incidence are enumerated in

Table 8 and Table 9 respectively. As we can notice, the specular reflectance in reflective materials is not a very strong function of the angle of incidence angle whereas in the case of refractive thin films or borosilicate glass, transmittance is a very strong function of the angle of incidence due to the Fresnel reflection losses involved.

Table 7 The optical properties of BK7 glass and various plastics used in dielectric solid fill solar concentrators.

Material	**Refractive Index - n_d (at λ=587.56 nm)**	**Abbe Number - V_d**	**Temperature Coefficient - dn/dT per °K**
PMMA	1.4918	57.4	-0.000105
PS	1.5905	30.9	-0.000140
PC	1.5855	29.9	-0.000107
SA	1.5674	34.8	-0.000110
BK7	1.5168	64.2	-0.000170

Table 8 The transmittance of a few solar concentrator materials.

T_{solar}	**0°**	**15°**	**45°**	**60°**
ETFE100µm	0.913	0.910	0.889	0.831
FEP100µm	0.946	0.944	0.932	0.877
Borosilicate 3.3mm	0.921	-	-	-
BorosilicateAR 3.3mm	0.950	0.949	0.940	0.880

Table 9 Specular reflectance of a few solar concentrator materials.

$R_{specular,solar}$	**15°**	**45°**	**60°**
Ag Glass 4mm (2014)	0.942	0.935	0.934
Ag Glass 2mm (2013)	0.941	-	-
Ag Glass 1mm (2008)	-	0.934	-
Ag Film#1	0.926	0.922	0.913
Ag Film#2	0.908	0.901	0.893
Al Film	0.895	0.898	0.894
Ag Sheet#1	0.939	0.941	0.944
Ag Sheet#2	0.948	0.949	0.949
Ag Sheet#3	0.954	0.951	0.952
Al Sheet	0.860	0.865	-

APPENDIX I: FRESNEL EQUATIONS

The dispersion equation of a material establishes its refractive index (n) as a function of wavelength (λ), therefore, the values of reflectance and transmittance change with respect to the wavelength of the incident radiation. For instance, PMMA material is governed by the following dispersion equation (within the wavelengths, λ = 0.42 - 1.62 μm) [51].

$$n^2 = 2.1778 + 6.1209 \times 10^{-3}\lambda^2 - 1.5004 \times 10^{-3}\lambda^4 + 2.3678 \times 10^{-2}\lambda^{-2} - 4.2137 \times 10^{-3}\lambda^{-4} + 7.3417 \times 10^{-4}\lambda^{-6} - 4.5042 \times 10^{-5}\lambda^{-8}$$

However, all throughout this paper, a spectral average of the transmittance and reflectance values over the solar spectrum (0.3 μm - 4 μm) are considered for simplification of the analysis. Also, other optical interactions such as scattering, absorption etc. are comparatively negligible. The following are the Fresnel equations used to evaluate the transmittance and reflectance values at various angles of incidence.

$n_{i,\lambda}$= refractive index of incident medium at a given wavelength (λ)

$n_{t,\lambda}$= refractive index of the transmitted medium at a given wavelength (λ)

$\theta_{i,\lambda}$= angle of incidence with respect to the surface normal

$\theta_{t,\lambda}$= transmitted angle or the angle of refraction $=\sin^{-1}\left(\frac{n_{i,\lambda}\sin(\theta_{i,\lambda})}{n_{t,\lambda}}\right)$ (Snell's law)

ρ_λ= ratio of refractive indices = $\frac{n_{t,\lambda}}{n_{i,\lambda}}$

m_λ= magnification at the interface = $\left(\frac{\cos\theta_{t,\lambda}}{\cos\theta_{i,\lambda}}\right)$

The subscripts ⊥ and ∥ represents perpendicular and parallel polarized radiation respectively.

$r_{\perp,\lambda}$, $r_{\parallel,\lambda}$ = reflection coefficients; where $r_{\perp,\lambda} = \frac{(1-\rho\, m)_\lambda}{(1+\rho\, m)_\lambda}$ and $r_{\parallel,\lambda} = \frac{(m-\rho\,)_\lambda}{(m+\rho\,)_\lambda}$

$t_{\perp,\lambda}$, $t_{\parallel,\lambda}$ = transmission coefficients; where $t_{\perp,\lambda} = \frac{2}{(1+\rho\, m)_\lambda}$ and $t_{\parallel,\lambda} = \frac{2}{(m+\rho\,)_\lambda}$

Reflectance, R= $\left(\frac{Reflected\ power}{Incident\ power}\right)$ and Transmittance, T= $\left(\frac{Transmitted\ power}{Incident\ power}\right)$

$$R_{\perp,\lambda} = \left(r_{\perp,\lambda}\right)^2 \quad \& \quad T_{\perp,\lambda} = \rho_\lambda\, m_\lambda \left(t_{\perp,\lambda}\right)^2$$
$$R_{\parallel,\lambda} = \left(r_{\parallel,\lambda}\right)^2 \qquad T_{\parallel,\lambda} = \rho_\lambda\, m_\lambda \left(t_{\parallel,\lambda}\right)^2$$

$$R_{avg,\lambda} = \frac{R_{\perp,\lambda} + R_{\parallel,\lambda}}{2} \quad \& \quad T_{avg,\lambda} = \frac{T_{\perp,\lambda} + T_{\parallel,\lambda}}{2}$$

$$R_{avg} = \frac{\sum_{\lambda=0.3}^{4\mu m} R_{avg,\lambda}}{N} \quad \& \quad T_{avg} = \frac{\sum_{\lambda=0.3}^{4\mu m} T_{avg,\lambda}}{N}$$

Where ‘N’ is the number of discrete wavelength values between 0.3 and 4 µm (solar spectrum). In case of PMMA material, 241 wavelength values were selected between 0.42 and 1.62 µm to evaluate R_{avg} and T_{avg} at various angles of incidence using the above mentioned Fresnel equations.

BIBLIOGRAPHY

[1] H. Mousazadeh, A. Keyhani, A. Javadi, H. Mobli, K. Abrinia, and A. Sharifi, “A review of principle and sun-tracking methods for maximizing solar systems output,” *Renew. Sustain. Energy Rev.*, vol. 13, no. 8, pp. 1800–1818, 2009.

[2] F. A. Janet L. Sawin, Kristin Seyboth, Freyr Sverrisson, Adam Brown, Bärbel Epp, Anna Leidreiter, Christine Lins, Hannah E. Murdock, Evan Musolino, T. T. K. Ksenia Petrichenko, Timothy C. Farrell, Aristeidis Tsakiris, Jonathan Skeen, and Benjamin Sovacool, “Renewables 2016 Global Status Report,” Paris, 2016.

[3] P. Gleckman, J. O’Gallagher, and R. Winston, “Concentration of sunlight to solar-surface levels using non-imaging optics,” *Nature*, vol. 339, no. 6221, pp. 198–200, May 1989.

[4] R. Leutz and A. Suzuki, *Nonimaging Fresnel lenses: design and performance of solar concentrators*, vol. 83. Springer, 2012.

[5] D. Y. Goswami, F. Kreith, and J. F. Kreider, *Principles of solar engineering*. CRC Press, 2000.

[6] A. Rabl, “Comparison of solar concentrators,” *Sol. Energy*, vol. 18, no. 2, pp. 93–111, 1976.

[7] R. Winston, “Principles of solar concentrators of a novel design,” *Sol. Energy*, vol. 16, no. 2, pp. 89–95, Oct. 1974.

[8] R. Winston and H. Hinterberger, “Principles of cylindrical concentrators for solar energy,” *Sol. Energy*, vol. 17, no. 4, pp. 255–258, Sep. 1975.

[9] D. P. Grimmer, “A comparison of compound parabolic and simple parabolic concentrating solar collectors,” *Sol. Energy*, vol. 22, no. 1, pp. 21–25, 1979.

[10] A. Rabl, “Solar concentrators with maximal concentration for cylindrical absorbers,” *Appl. Opt.*, vol. 15, no. 7, pp. 1871–1873, Jul. 1976.

[11] W. R. McIntire, “Truncation of nonimaging cusp concentrators,” *Sol. Energy*, vol. 23, no. 4, pp. 351–355, 1979.

[12] M. M. Shapiro, “Non-focussing solar concentrators of easy manufacture,” *Sol. Energy*, vol. 19, no.

2, pp. 211–213, 1977.

[13] R. E. Jones and G. C. Anderson, “Optical properties of compound circular arc concentrators,” *Sol. Energy*, vol. 21, no. 2, pp. 149–151, 1978.

[14] E. M. Kritchman, “Second-stage CEC concentrator,” *Appl. Opt.*, vol. 21, no. 4, pp. 751–754, Feb. 1982.

[15] I. R. Edmonds, “Prism-coupled compound parabola: a new ideal and optimal solar concentrator,” *Opt. Lett.*, vol. 11, no. 8, pp. 490–492, Aug. 1986.

[16] J. M. Gordon and A. Rabl, “Nonimaging compound parabolic concentrator-type reflectors with variable extreme direction,” *Appl. Opt.*, vol. 31, no. 34, pp. 7332–7338, Dec. 1992.

[17] J. J. O’Gallagher, “Retrospective on 30 years of nonimaging optics development for solar energy at the University of Chicago,” *Proc. SPIE*, vol. 9955. pp. 995504–995520, 2016.

[18] M. Khamooshi, H. Salati, F. Egelioglu, A. Hooshyar Faghiri, J. Tarabishi, and S. Babadi, “A review of solar photovoltaic concentrators,” *Int. J. Photoenergy*, vol. 2014, p. 17, 2014.

[19] K.-K. Chong, S.-L. Lau, T.-K. Yew, and P. C.-L. Tan, “Design and development in optics of concentrator photovoltaic system,” *Renew. Sustain. Energy Rev.*, vol. 19, pp. 598–612, 2013.

[20] R. Winston, J. C. Miñano, P. Benítez, N. Shatz, and J. C. Bortz, *Nonimaging Optics*. Elsevier, 2005.

[21] H. Ries and A. Rabl, “Edge-ray principle of nonimaging optics,” *J. Opt. Soc. Am. A*, vol. 11, no. 10, pp. 2627–2632, 1994.

[22] O. Dross, R. Mohedano, P. Benitez, J. C. Minano, J. Chaves, J. Blen, M. Hernández, and F. Muñoz, “Review of SMS design methods and real-world applications,” in *Optical Science and Technology, the SPIE 49th Annual Meeting*, 2004, pp. 35–47.

[23] J. C. Minano, “Poisson brackets method of design of nonimaging concentrators: a review,” *Proc. SPIE*, vol. 2016. pp. 98–108, 1993.

[24] J. Chaves, *Introduction to Nonimaging Optics, Second Edition*. CRC Press, 2015.

[25] J. M. Gordon, “Complementary construction of ideal nonimaging concentrators and its applications,” *Appl. Opt.*, vol. 35, no. 28, pp. 5677–5682, Oct. 1996.

[26] H. E. I. Khonkar and A. A. M. Sayigh, “Raytrace for compound parabolic concentrator,” *Renew. Energy*, vol. 5, no. 1–4, pp. 376–383, Aug. 1994.

[27] “Optical software: which program is right for me?,” 2006. [Online]. Available: http://optics.org/article/25404. [Accessed: 01-Jan-2015].

[28] D. Chemisana, M. Ibáñez, and J. Barrau, “Comparison of Fresnel concentrators for building integrated photovoltaics,” *Energy Convers. Manag.*, vol. 50, no. 4, pp. 1079–1084, Apr. 2009.

[29] J.-S. Lin, W.-C. Huang, H.-C. Hsu, M.-W. Chang, and C.-P. Liu, “A study for the special Fresnel lens for high efficiency solar concentrators,” in *Nonimaging Optics and Efficient Illumination Systems II*, 2005, vol. 5942, p. 59420X1-59420X9.

[30] Lambda Research Corporation, “TracePro 7.8 User’s Manual,” 2016. [Online]. Available: http://www.lambdares.com/CustomerSupportCenter/TraceProDownload/TracePro_User_Manual.pdf. [Accessed: 11-Nov-2016].

[31] E. Hecht and A. Zajac, *Optics 4th (International) Edition*. Addison Wesley Publishing Company, San Francisco, 2002.

[32] A. I. Lvovsky, “Fresnel Equations,” in *Encyclopedia of Optical Engineering*, pp. 1–6.

[33] National Renewable Energy Laboratory (NREL), “National Solar Radiation Data Base 1991- 2005 Update: Typical Meteorological Year 3,” 2008. [Online]. Available: http://rredc.nrel.gov/solar/old_data/nsrdb/1991-2005/tmy3/. [Accessed: 01-Jan-2016].

[34] “Standard Tables for Reference Solar Spectral Irradiances: Direct Normal and Hemispherical on 37° Tilted Surface.” ASTM International, 2012.

[35] Lord Rayleigh, “On Reflection of Vibrations at the Confines of two Media between which the Transition is Gradual,” *Proc. London Math. Soc.*, vol. s1-11, no. 1, pp. 51–56, 1879.

[36] H. K. Raut, V. A. Ganesh, A. S. Nair, and S. Ramakrishna, “Anti-reflective coatings: A critical, in-depth review,” *Energy Environ. Sci.*, vol. 4, no. 10, pp. 3779–3804, 2011.

[37] Y.-F. Huang, S. Chattopadhyay, Y.-J. Jen, C.-Y. Peng, T.-A. Liu, Y.-K. Hsu, C.-L. Pan, H.-C. Lo, C.-H. Hsu, Y.-H. Chang, and others, “Improved broadband and quasi-omnidirectional anti-

reflection properties with biomimetic silicon nanostructures," *Nat. Nanotechnol.*, vol. 2, no. 12, pp. 770–774, 2007.

[38] J. A. Dobrowolski, D. Poitras, P. Ma, H. Vakil, and M. Acree, "Toward perfect antireflection coatings: numerical investigation," *Appl. Opt.*, vol. 41, no. 16, pp. 3075–3083, Jun. 2002.

[39] R. Winston, "Dielectric compound parabolic concentrators," *Appl. Opt.*, vol. 15, no. 2, pp. 291–292, Feb. 1976.

[40] W. T. Xie, Y. J. Dai, R. Z. Wang, and K. Sumathy, "Concentrated solar energy applications using Fresnel lenses: A review," *Renew. Sustain. Energy Rev.*, vol. 15, no. 6, pp. 2588–2606, Aug. 2011.

[41] J. H. Goodman, "Building Interior Evacuated Tubes and Reflectors," in *Solar 2009 ASES conference*, 2009.

[42] J. Blanco, S. Malato, P. Fernández, A. Vidal, A. Morales, P. Trincado, J. . Oliveira, C. Minero, M. Musci, C. Casalle, M. Brunotte, S. Tratzky, N. Dischinger, K.-H. Funken, C. Sattler, M. Vincent, M. Collares-Pereira, J. . Mendes, and C. . Rangel, "Compound parabolic concentrator technology development to commercial solar detoxification applications," *Sol. Energy*, vol. 67, no. 4–6, pp. 317–330, 1999.

[43] J. M. Gordon, "Nonimaging optical designs for laser fiber optic surgery," *Opt. Eng.*, vol. 37, no. 2, pp. 539–542, 1998.

[44] Z. S. Lu, R. Z. Wang, Z. Z. Xia, X. R. Lu, C. B. Yang, Y. C. Ma, and G. B. Ma, "Study of a novel solar adsorption cooling system and a solar absorption cooling system with new CPC collectors," *Renew. Energy*, vol. 50, pp. 299–306, 2013.

[45] M. J. Clifford and D. Eastwood, "Design of a novel passive solar tracker," *Sol. Energy*, vol. 77, no. 3, pp. 269–280, Sep. 2004.

[46] V. Poulek, "Testing the new solar tracker with shape memory alloy actors," in *Photovoltaic Energy Conversion, 1994., Conference Record of the Twenty Fourth. IEEE Photovoltaic Specialists Conference - 1994, 1994 IEEE First World Conference on*, 1994, vol. 1, pp. 1131–1133 vol.1.

[47] F. H. Klotz, H. D. Mohring, C. Gruel, M. A. Abella, J. Sherborne, T. Bruton, and P. Tzanetakis,

"Field test results of the Archimedes Photovoltaic V-Trough concentrator system," in *Proceedings of the 17th European Photovoltaic Solar Energy Conference and Exhibition, Munich, Germany*, 2001, pp. 492–495.

[48] M. M. P. Sánchez, D. B. Tamayo, and R. H. C. Estrada, "Design and construction of a dual axis passive solar tracker, for use on Yucatán," in *ASME 2011 5th International Conference on Energy Sustainability*, 2011, pp. 1341–1346.

[49] R. R. Shannon, *The art and science of optical design*. Cambridge University Press, 1997.

[50] P. Good, T. Cooper, M. Querci, N. Wiik, G. Ambrosetti, and A. Steinfeld, "Spectral reflectance, transmittance, and angular scattering of materials for solar concentrators," *Sol. Energy Mater. Sol. Cells*, vol. 144, pp. 509–522, 2016.

[51] G. Beadie, M. Brindza, R. A. Flynn, A. Rosenberg, and J. S. Shirk, "Refractive index measurements of poly(methyl methacrylate) (PMMA) from 0.4 – 1.6 μm," *Appl. Opt.*, vol. 54, no. 31, pp. F139--F143, Nov. 2015.

CURRICULUM VITAE

Graduate College

University of Nevada, Las Vegas

Srikanth Madala

Degrees

- Bachelor of Technology, Mechanical Engineering, 2007

  Jawaharlal Nehru Technological University (JNTU), Hyderabad, India
- Master of Sciences, Mechanical Engineering, 2008

  University of Florida, Gainesville, USA.

Publications and Conferences

[1] Madala, S., & Boehm, R. F. (2016). Effect of reflection losses on stationary dielectric-filled nonimaging concentrators. *Journal of Photonics for Energy*, *6*(4), 047002-047002.

[2] Madala, S., & Boehm, R. F. (2016). A review of nonimaging solar concentrators for stationary and passive tracking applications. *Renewable and Sustainable Energy Reviews*, Advance online publication. doi:10.1016/j.rser.2016.12.058

[3] Sadineni, S. B., Madala, S., & Boehm, R. F. (2011). Passive building energy savings: A review of building envelope components. *Renewable and Sustainable Energy Reviews*, *15*(8), 3617-3631.

[4] Sadineni, S. B., Madala, S., & Boehm, R. F. (2012, July). A Cost Effective Solar Tracker and Performance Monitoring System for Utility Scale Photovoltaic Installations. In *ASME 2012 6th International Conference on Energy Sustainability collocated with the ASME 2012 10th International Conference on Fuel Cell Science, Engineering and Technology* (pp. 965-977). American Society of Mechanical Engineers.

[5] Realmuto, J. D., Sadineni, S. B., Madala, S., & Boehm, R. F. (2011, January). Experimental Comparison and Economic Analysis of PV Technologies for Utility Scale Installations. In *ASME 2011 5th International Conference on Energy Sustainability* (pp. 1333-1339). American Society of Mechanical Engineers.

[6] Atallah, F., Madala, S., Sadineni, S. B., & Boehm, R. F. (2011, January). Optimization of a Coupled Vapor Compression and Absorption Cooling System Driven by Gas Fueled IC Engine. In *ASME 2011 5th International Conference on Energy Sustainability* (pp. 369-374). American Society of Mechanical Engineers.

[7] Madala, S., and Boehm, R. F. (2017). Design improvements in stationary nonimaging solar concentrators. *Solar Energy,* Publication under review by the authors.

Dissertation Title

Stationary nonimaging concentrators – a comprehensive study and design improvements

Dissertation Examination Committee

Chairperson, Dr. Robert F. Boehm, Ph.D.

Committee Member, Dr. Yi-Tung Chen, Ph.D.

Committee Member, Dr. Woosoon Yim, Ph.D.

Committee Member, Dr. Yahia Baghzouz, Ph.D.

Graduate College Representative, Dr. Rama Venkat, Ph.D.